

4 **Extracellular matrix mechanical cues regulate lipid metabolism through Lipin-1 and SREBP**

5 Patrizia Romani<sup>1</sup>, Irene Brian<sup>1</sup>, Giulia Santinon<sup>1</sup>, Arianna Pocaterra<sup>1</sup>, Matteo Audano<sup>2</sup>, Silvia Pedretti<sup>2</sup>,  
6 Samuel Mathieu<sup>3,4</sup>, Mattia Forcato<sup>5</sup>, Silvio Bicciato<sup>5</sup>, Jean-Baptiste Manneville<sup>3,4</sup>, Nico Mitro<sup>2</sup> & Sirio  
7 Dupont<sup>1\*</sup>

8  
9 <sup>1</sup>Department of Molecular Medicine (DMM), University of Padua, Padua, Italy

10 <sup>2</sup>Department of Pharmacological and Biomolecular Sciences (DiSFeB), University of Milan, Milan,  
11 Italy

12 <sup>3</sup>Institut Curie, PSL Research University, CNRS UMR144, Paris, France

13 <sup>4</sup>Sorbonne Universités, UPMC University Paris 06, CNRS UMR144, Paris, France

14 <sup>5</sup>Department of Life Sciences, University of Modena and Reggio Emilia, Modena, Italy

15  
16 \*correspondence: [sirio.dupont@unipd.it](mailto:sirio.dupont@unipd.it)  
17

18 **Extracellular matrix (ECM) mechanical cues have powerful effects on cell proliferation,**  
19 **differentiation and death. Here, starting from an unbiased metabolomics approach, we identified**  
20 **synthesis of neutral lipids as a general response to mechanical signals delivered by cell-matrix**  
21 **adhesions. Extracellular physical cues reverberate on the mechanical properties of the Golgi**  
22 **apparatus and regulate the Lipin-1 phosphatidate phosphatase. Conditions of reduced**  
23 **actomyosin contractility lead to inhibition of Lipin-1, accumulation of SCAP/SREBP to the Golgi**  
24 **apparatus and activation of SREBP transcription factors, in turn driving lipid synthesis and**  
25 **accumulation. This occurs independently of YAP/TAZ, mTOR and AMPK, and in parallel to the**  
26 **feedback control by sterols. Regulation of SREBP can be observed in a stiffened diseased tissue,**  
27 **and contributes to the pro-survival activity of ROCK inhibitors in pluripotent stem cells. We**  
28 **thus identify a general mechanism centered on Lipin-1 and SREBP that links the physical cell**  
29 **microenvironment to a key metabolic pathway.**

30

## 31 **Introduction**

32 Each tissue has a specific composition of its extracellular matrix (ECM), which is associated to  
33 distinctive physical and mechanical properties. These mechanical properties are important for tissue  
34 structure, but also control cell function in physiology and disease<sup>1,2</sup>. Cells sense the mechanical  
35 properties of the ECM through integrin receptors, and measure them by adjusting the contractility of  
36 their F-actin cytoskeleton: contractility is maximal when cells are free to spread on stiff ECM substrata,  
37 while it is progressively decreased on a soft ECM or in conditions of limited spreading. This is  
38 sufficient to control the switch between proliferation, differentiation and death in very diverse cell  
39 types, by regulating intracellular signaling pathways such as YAP/TAZ<sup>3,4</sup> and SRF<sup>5,6</sup>. In support of this  
40 model, inhibition of key players that maintain F-actin contractility including the small GTPase RHO,  
41 ROCK (RHO kinase), MLCK (myosin light chain kinase) and non-muscle myosin (NMII) induce  
42 similar responses to a soft ECM<sup>1</sup>. Yet, what other general aspects of cell biology are regulated by  
43 mechanical cues, and through which mechanism(s), remain largely unexplored. This is especially true  
44 in the case of metabolism, a fundamental engine that is constantly remodeled to match the energetic  
45 and biosynthetic requirements of the cell, whose connections to mechanical cues are only starting to  
46 emerge<sup>7,8</sup>.

47

## 48 **Actomyosin regulates lipid metabolism**

49 To test in an unbiased manner the possibility that actomyosin contractility regulates metabolism we  
50 compared by global metabolomics cells in conditions of high contractility (i.e. plated on plastics) with  
51 cells in conditions of low contractility, by inhibiting ROCK and MLCK. Analysis of steady-state levels  
52 of multiple metabolites indicated clear differences between controls and treated cells (Fig. **1a** and  
53 Supplementary Fig. **1a-e**); the most significant and quantitative changes, which were maintained or  
54 increased between 6 and 24 hours, were the accumulation of several lipid molecules (Supplementary  
55 Fig. **1e** and Ref.<sup>9</sup>).

56 We validated this initial observation with a targeted lipidomic analysis at 24 hours, which  
57 confirmed accumulation of triglycerides, diacylglycerols, lyso-phospholipids and ceramides, while  
58 many other lipid species remained overall unchanged (Fig. **1b-d**, Supplementary Fig. **1f-h** and Ref.<sup>9</sup>).

59 This was accompanied by increased free and total fatty acids and cholesterol in cell extracts (Fig. **1e,f**),  
60 and by a corresponding accumulation of cholesterol and neutral lipids in fixed cells (by Filipin and Oil-  
61 Red-O stains, respectively – Fig. **1g**, Supplementary Fig. **1i-k**). Such accumulation was visible after 6  
62 hours of treatment, and sustained up to 48 hours (Supplementary Fig. **1l**). A similar effect was observed  
63 by replacing Y27632 with Fasudil, an alternative ROCK inhibitor, or by using Y27632 or ML7  
64 inhibitors alone (Fig. **1g**). Accumulation of lipids was mainly due to increased synthesis, because it was  
65 impaired in cells where rate-limiting enzymes of cholesterol and fatty-acid synthesis were inhibited by  
66 Cerivastatin or TOFA (Fig. **1g**). Finally, lipid accumulation was a general response to ECM mechanical  
67 cues and actomyosin contractility because expression of the RHO inhibitor C3, treatment of cells with  
68 the NMII small-molecule inhibitor Blebbistatin, or seeding cells on a soft vs. stiff fibronectin-coated  
69 polyacrylamide hydrogels induced a coherent accumulation of cholesterol and lipid droplets (Fig. **1h-i**).

70 We then extended these findings in multiple cell types including primary, immortalized, and  
71 transformed cells, of both epithelial and connective tissue origin, indicating that lipid accumulation is a  
72 widespread response to conditions of reduced actomyosin contractility (Fig. **1j,k** and Supplementary  
73 Fig. **1m,n**).

#### 74 75 **ECM mechanical cues regulate a genetic program for lipid synthesis**

76 Thinking of potential mechanisms underlying this metabolic shift, we tested an involvement of the  
77 Hippo pathway. YAP/TAZ are inhibited by reduced actomyosin contractility<sup>3,4</sup>, but their knockdown  
78 did not cause lipid accumulation comparable to ROCK/MLCK inhibition (Supplementary Fig. **2a**).

79 Similarly, stable TAZ-S4A active mutant expression was not sufficient to prevent lipid accumulation  
80 upon ROCK/MLCK inhibition (Supplementary Fig. **2b**). LATS1/2 Hippo kinases can be activated by

81 reduced actomyosin contractility<sup>10</sup>, but genetics indicated that LATS2 inhibits lipid metabolism<sup>11</sup>,  
82 which was incompatible with our results. This suggested the regulation of an alternative pathway that  
83 we sought to identify by performing microarray analysis of MCF10ATk1 cells treated with  
84 Y27632+ML7, followed by gene list enrichment analysis. As shown in Fig. **2a,b** we found a striking  
85 enrichment of signatures related to cholesterol and fatty acid synthesis among the upregulated genes,  
86 including many known SREBP1 and SREBP2 (sterol regulatory element binding proteins) targets,  
87 pointing to activation of these transcription factors<sup>12,13</sup>. We thus validated activation of SREBP1/2 by a  
88 luciferase reporter for SREBP transcriptional activity, by qPCR, and in multiple cell lines (Fig. **2c,d**  
89 and Supplementary Fig. **2d-f**). Importantly, we also observed a coherent induction of SREBP target  
90 genes in cells cultured on soft hydrogels (Fig. **2e-g**), while YAP/TAZ inhibition had no effects on  
91 SREBP activity (Supplementary Fig. **2g,h**). Of note, among the validated SREBP targets *LDLR* (*low*  
92 *density lipoprotein receptor*) expression correlated with increased fatty acid uptake (Supplementary  
93 Fig. **2i**), and *ACSS2* (*acyl-CoA synthetase short chain family member 2*) with increased usage of acetate  
94 for lipid synthesis<sup>14</sup> (Supplementary Fig. **2j**).

95

### 96 **ECM mechanical cues control lipid synthesis through direct regulation of SREBP1/2 activity**

97 SREBP are produced as transmembrane proteins resident in the ER (endoplasmic reticulum) (see  
98 model in Supplementary Fig. **3a**): in the presence of sterols and fatty acids, SCAP (SREBP cleavage-  
99 activating protein) and Insig (insulin-induced gene) proteins bind SREBP and limit their transport to  
100 the Golgi apparatus; in absence of lipids, conformational changes in SCAP and Insig enable the  
101 quantitative transport of SCAP and SREBP to the Golgi, where SREBP are processed by the S1P (site-  
102 1 protease) and S2P (site-2 protease) Golgi-resident enzymes. This in turn releases the cytoplasmic  
103 portion of SREBP that is free to accumulate into the nucleus to regulate gene transcription<sup>12,13</sup>.

104 Prompted by the observation that mechanical cues regulate SREBP activity, we sought to  
105 causally link SREBP activity with the effects of mechanical cues. As shown in Fig. **3a-c** and  
106 Supplementary Fig. **3b,c** knockdown of SREBP1/2 inhibited expression of lipid enzymes and lipid  
107 accumulation in response to Y27632+ML7 and to a soft hydrogel. We then probed endogenous  
108 SREBP2 localization and observed an early concentration to the Golgi apparatus (2 hours), closely  
109 followed by nuclear accumulation (4-6 hours), upon treatment with ROCK/MLCK inhibitors (Fig. **3d**  
110 and Supplementary Fig. **3d-g**). Nuclear accumulation of SREBP2 started to fade at 24 hours and  
111 became almost undetectable at 48 hours of treatment (Fig. **3d**), likely due to accumulation of lipids  
112 eventually restraining SREBP activation. Moreover, nuclear accumulation was reversible, since

113 washout of the inhibitors led to the rapid disappearance of nuclear SREBP2 (Fig. 3d). In keeping with a  
114 general effect of mechanical cues, nuclear SREBP2 was observed upon transfection of the C3 RHO  
115 inhibitor, treatment with Blebbistatin, and on soft hydrogels (Fig. 3d and Supplementary Fig. 3f,g).  
116 This was associated with accumulation of cleaved SREBP1 and SREBP2 in nuclear extracts (Fig. 3e  
117 and Supplementary Fig. 3h). In line with a direct effect, nuclear accumulation of SREBP2 occurred in  
118 absence of protein synthesis (Fig. 3f,g and Supplementary Fig. 3i,j). Finally, ROCK/MLCK inhibitors  
119 could not stimulate further *LDLR-luciferase* in cells engineered to express only a mature form of  
120 SREBP2 (Fig. 3h), indicating regulation of SREBP2 at the level of cleavage and not of nuclear  
121 stability.

122

### 123 **Inhibition of SREBP activity by pathological tissue stiffness**

124 To find evidence that this regulation also occurs in vivo, we queried gene expression data obtained by  
125 comparing patient-matched normal skin with keloid scars<sup>15</sup>, a fibroproliferative disorder characterized  
126 by increased tissue stiffness and whose expansion is linked to mechanical stress<sup>16,17</sup>. Strikingly, several  
127 SREBP target genes were consistently and uniformly downregulated in stiffened keloids across all  
128 patients, supporting our model (Fig. 3i). Of note, this finding nicely parallels the so-far unexplained  
129 decrease in lipids and cholesterol-esters observed in keloids<sup>18</sup>. As a control, we also found upregulation  
130 of several YAP/TAZ target genes (Fig. 3i), in line with stiffness-induced YAP/TAZ activity during  
131 fibrosis<sup>19,20</sup>. Thus, cytoskeletal tension is a relevant input to regulate SREBP in vitro and in at least one  
132 human pathological tissue.

133

### 134 **ECM mechanical cues regulate SCAP localization and function**

135 We next probed the subcellular localization of core SREBP regulators. While Insig1 and S1P remained  
136 correctly confined to the ER and the Golgi apparatus, respectively (Supplementary Fig. 4a,b), we  
137 observed translocation of SCAP to the Golgi apparatus by plating cells on soft hydrogels and after  
138 inhibition of RHO or ROCK/MLCK (Fig. 4a,b and Supplementary Fig. 4c). This was instrumental for  
139 the regulation of SREBP by mechanical cues, because both SCAP knockdown and treatment of cells  
140 with 25-hydroxycholesterol, a dominant inhibitor of SCAP transport<sup>21</sup>, decreased SREBP activation  
141 (Fig. 4c,e and Supplementary Fig. 4d). In line, treating cells with the S1P inhibitor PF429242 also  
142 prevented activation of SREBP (Fig. 4d,e). This indicates that actomyosin contractility prevents  
143 accumulation of SCAP/SREBP to the Golgi apparatus and the exposure of SREBP to Golgi proteases.

144

145 **Lipid synthesis contributes to the beneficial effects of ROCK inhibitors in hPSC**

146 To expand the functional implications of these findings we used human Pluripotent Stem Cells (hPSC).  
147 These cells require treatment with the Y27632 ROCK inhibitor to survive single-cell dissociation,  
148 while they thrive without inhibitor once they have attached to the substrate<sup>22,23</sup>. We thus tested the idea  
149 that Y27632 might promote survival of hPSC by enhancing lipid synthesis. We first confirmed that  
150 Y27632 induces lipid accumulation also in these cells (Supplementary Fig. **4e**). We then challenged  
151 Y27632-induced survival of hPSC seeded as single cells by using very low doses of lipid synthesis  
152 inhibitors (Cerivastatin and TOFA), and found that hPSC did not survive (Fig. **4f**, single cells); the  
153 same dose of inhibitors was instead inconsequential for cell survival of already-established hPSC  
154 colonies, when Y27632 is not required (Fig. **4f**, colonies). In line, both treatment of cells with 25-  
155 hydroxycholesterol and transfection of SREBP1/2 siRNAs impaired Y27632-induced single-cell  
156 survival (Fig. **4g,h**). These results suggest that isolated hPSC are highly dependent on lipid synthesis,  
157 and that ROCK inhibition promotes their survival, at least in part, by sustaining SREBP activity.

158

159 **Uncoupling actomyosin contractility from intracellular cholesterol trafficking**

160 One possibility to explain our findings is that reduced actomyosin contractility leads to reduced levels  
161 of sterols at the ER because of decreased transport of extracellular cholesterol from the  
162 endosome/lysosome to the ER by the NPC1 transporter<sup>12,13</sup>. We excluded this scenario based on the  
163 following observations: (i) cholesterol accumulation in response to Y27632+ML7 was decreased in  
164 cells with inhibited synthesis or with SREBP1/2 knockdown (see above), indicating it is a secondary  
165 effect; (ii) cholesterol accumulation occurred after SREBP activation, and with a delayed kinetics  
166 compared to inhibition of the NPC1 transporter with U18666A (Supplementary Fig. **5a**); (iii) while  
167 U18666A induced accumulation of cholesterol in LAMP2-encircled lysosomal structures, as expected,  
168 only few Y27632+ML7-induced cholesterol dots were positive for LAMP2 (Supplementary Fig. **5b**);  
169 (iv) treatment with Y27632+ML7, at difference with U18666A or with serum (and, thus, LDL-  
170 cholesterol) deprivation, did not cause concentration of the ER cholesterol-sensing protein OSBP to the  
171 Golgi apparatus at early time-points<sup>24,25</sup> (Supplementary Fig. **5c**).

172

173 **Linking actomyosin contractility to the Lipin-1/ARF1 SREBP-regulatory axis**

174 Looking for alternative mechanisms, we reasoned that among the known SREBP-regulatory inputs, two  
175 act independently of sterol levels: ARF1 and Lipin-1. The ARF1 (ADP ribosylation factor 1) small G  
176 protein regulates Golgi dynamics<sup>26,27</sup>, and inhibits SREBP<sup>28-30</sup>. The precise mechanism remained

177 incompletely understood, because Walker and colleagues showed that ARF1 prevents S1P from  
178 shuttling to the ER, while Nakayama and colleagues showed that the ARF1 effector COPI prevents  
179 accumulation of SCAP/SREBP to the Golgi. Lipin-1 is a phosphatase that converts phosphatidates into  
180 diacylglycerols at cytoplasmic membranes<sup>31</sup>, and also an inhibitor of SREBP activity<sup>29,32</sup>. Interestingly,  
181 ARF1 recruitment to the Golgi apparatus and formation of COPI-coated vesicles requires  
182 diacylglycerols<sup>33-36</sup>, such that inhibition of Lipin-1 activity can cause ARF1 dissociation from Golgi  
183 membranes and ARF1 inhibition<sup>29,35</sup>. This suggested us that reduced actomyosin contractility might  
184 induce SREBP activity by inhibiting Lipin-1/ARF1 (see model in Supplementary Fig. **5d**).

185 We first verified that inhibition of Lipin-1, ARF1 or COPI induce SREBP activation, SCAP  
186 accumulation at the Golgi apparatus and lipid accumulation in our systems (Fig. **5a-f** and  
187 Supplementary Fig. **5e**). We then indirectly gauged Lipin-1 activity by monitoring its association with  
188 microsomes<sup>37,38</sup> or by monitoring Golgi membrane diacylglycerol (DG) content with the DG-binding  
189 domain of PKD1 (GFP-PKD-KD)<sup>35,39,40</sup>, and found that inhibition of ROCK/MLCK rapidly caused  
190 Lipin-1 dissociation from microsomes (Fig. **5g**) and decreased GFP-PKD-KD co-localization with the  
191 Golgi apparatus (Fig. **5h**). ROCK/MLCK inhibition also decreased ARF1 activity (Fig. **5i**) and ARF1  
192 recruitment to the Golgi apparatus (Fig. **5j**). Moreover, both Lipin-1 and ROCK/MLCK inhibition  
193 induce similar remodeling of Golgi morphology at late time-points (Supplementary Fig. **5f,g**), a  
194 phenotype previously observed in cells depleted of GBF1/ARF1<sup>28</sup>. We did not observe a general  
195 redistribution of a fluorescent KDEL reporter (Supplementary Fig. **5h**), indicating overall intact  
196 transports between ER and Golgi. Collectively, our data indicate that mechanical cues control Lipin-1  
197 activity, causing altered ARF1-dependent trafficking of SCAP/SREBP between the Golgi and the ER.

198

### 199 **Actomyosin contractility controls SREBP through Lipin-1, but independently from** 200 **AMPK/mTOR**

201 We then explored how Lipin-1 is regulated. Lipin-1 activity and association to cytoplasmic membranes  
202 can be inhibited by phosphorylation<sup>32,37,38</sup>. We checked Lipin-1 overall phosphorylation levels, but we  
203 did not observe major changes of the Lipin-1 migratory pattern (Fig. **6a**). We also monitored Lipin-1  
204 subcellular localization by immunofluorescence, and found that reduced contractility partially shifted  
205 FLAG-Lipin-1 towards the nucleus (Fig. **6b,c**). Nuclear Lipin-1 has been associated with inactivation  
206 of SREBP<sup>32</sup>; since we observed a partial nuclear accumulation of Lipin-1 in conditions of active  
207 SREBP, we then wondered what pool of Lipin-1 was relevant in our cells. For this we compared wild-  
208 type Lipin-1 (WT) with a nuclear phospho-mutant (17S/A) and with Lipin-1 isoforms that we designed

209 to constitutively associate with ER/Golgi membranes (MB-Lipin-1 and MB\*-Lipin-1 - see Fig. **6c**), and  
210 used these to challenge the effects of reduced contractility. While the WT and 17S/A mutant were  
211 inactive, expression of membrane-associated Lipin-1 counteracted SREBP activity (Fig. **6d,e**) and lipid  
212 accumulation (Fig. **6f**). Also the SUMOylation<sup>41</sup> and acetylation<sup>42</sup> Lipin-1 mutants were inactive in the  
213 same assay (Supplementary Fig. **6a**). Collectively, these results indicate that reduced contractility  
214 inhibits the affinity of Lipin-1 for ER/Golgi membranes, leading to nuclear localization of Lipin-1 as  
215 secondary effect. This occurs independently from mTOR, a known Lipin-1 regulatory input  
216 (Supplementary Fig. **6b,c**), and also from AMPK, a main metabolic regulator (Supplementary Fig.  
217 **6d,e**).

### 218

### 219 **The Golgi apparatus responds to extracellular and intracellular forces**

220 We finally sought to obtain some insight into how extracellular mechanical cues influence signaling at  
221 the Golgi apparatus. Transmission of forces from the ECM entail activation of signaling molecules at  
222 focal adhesions<sup>1</sup> but also occur in a direct fashion, for example by stretching the plasma membrane, or  
223 owing to anchoring of stress fibers to the nuclear lamina<sup>43,44</sup>. Whether the Golgi apparatus might  
224 respond in a similar fashion has not been explored, but Golgi cisternae are embedded in a complex  
225 cytoskeletal network<sup>45,46</sup>, and the Golgi microenvironment is endowed of an intrinsic mechanical  
226 rigidity which depends on ROCK/MLCK<sup>47</sup>. To measure the response of Golgi rigidity to external  
227 physical cues we plated cells on small fibronectin-coated micropatterns, to which cells respond by  
228 decreasing actomyosin contractility<sup>48</sup>, and by accumulating SCAP to the Golgi apparatus (Fig. **7a**). We  
229 then measured Golgi rheology by pushing on the Golgi apparatus a cytoplasmic bead immobilized in a  
230 laser optical trap (see methods and Supplementary Fig. **7a**). Analysis of the averaged relaxation curves  
231 (Fig. **7b** and Supplementary Fig. **7b**) indicated a lower rigidity of the Golgi apparatus in micropatterned  
232 cells, apparent from reduction of the bead step amplitude, the rigidity index, and the frequency of bead  
233 ejection (Fig. **7c**). As a control, moving the bead away from the Golgi showed that the overall  
234 cytoplasmic stiffness is not altered (Supplementary Fig. **7c**). This experiment indicates that Golgi  
235 stiffness is coupled, directly or indirectly, to the mechanical properties of the ECM. Strikingly, with  
236 this set-up we also observed that direct application of force to the Golgi apparatus was sufficient to  
237 induce recruitment of the GFP-PKD-KD reporter (Fig. **7d,e**), in line with higher Lipin-1 activity in  
238 cells developing higher contractile forces (see above).

### 239

### 240 **Discussion**

241 Seminal work demonstrating that cells sense ECM mechanical cues set the array of bona-fide  
242 mechanoregulated phenotypes in vitro. Yet, what other general cell phenotypes are regulated by  
243 mechanical cues remains largely unexplored. Here we focused on cell metabolism and identified  
244 neutral lipid and cholesterol synthesis as a general response to reduced actomyosin contractility and to  
245 a soft ECM microenvironment. We propose that decreased extracellular forces reverberate on Golgi  
246 rheology and inactivate Lipin-1, causing alteration of diacylglycerol at the Golgi apparatus, reduced  
247 recruitment of ARF1, and ultimately leading to activation of SREBP1/2 transcription factors. As such,  
248 our data provide a missing upstream input for the Lipin-1 and ARF1 SREBP-regulatory axis, whose  
249 players were previously identified in *C. elegans*<sup>29</sup>, and validates the idea that continuous shuttling of  
250 SCAP/SREBP from the Golgi to the ER is a significant mechanism limiting their activation<sup>30</sup>. These  
251 findings led us to revisit the requirement of isolated human pluripotent stem cells for ROCK inhibition,  
252 that we found linked to the ability to sustain SREBP activity and lipid synthesis. We speculate this  
253 might underlie the beneficial effect of ROCK inhibition observed for isolation of other primary stem-  
254 cell populations<sup>49-51</sup>. These findings also indicate that physiological or pathological conditions leading  
255 to altered tissue stiffness may impact SREBP activity and lipid metabolism; strikingly, we could obtain  
256 a proof-of-principle for this in human keloid scars, providing a plausible explanation for reduced  
257 triglycerides and cholesteryl-esters<sup>18</sup>. Thus, we here identify an unexpected and widespread  
258 mechanoresponsive phenotype, and its main underlying mechanism. Our findings raise interesting  
259 questions on how Lipin-1 is regulated in this context; we speculate that Lipin-1 macromolecular  
260 complexes observed on supported lipid bilayers in vitro<sup>52</sup> are endowed of curvature-sensing ability,  
261 which might link Lipin-1 activity to the rheology of Golgi membranes and the cytoskeleton. In future,  
262 it will be interesting to test whether ECM mechanical cues affect other functions of the Golgi, of Lipin-  
263 1 signaling and of ARF1, and how these impact the response of normal and diseased tissues to  
264 mechanical cues.

265

## 266 **References**

- 267 1. Iskratsch, T., Wolfenson, H. & Sheetz, M. P. Appreciating force and shape—the rise of  
268 mechanotransduction in cell biology. *Nat. Rev. Mol. Cell Biol.* **15**, 825–833 (2014).
- 269 2. LeGoff, L. & Lecuit, T. Mechanical Forces and Growth in Animal Tissues. *Cold Spring Harbor*  
270 *Perspectives in Biology* **8**, a019232 (2015).
- 271 3. Dupont, S. *et al.* Role of YAP/TAZ in mechanotransduction. *Nature* **474**, 179–183 (2011).
- 272 4. Dupont, S. Role of YAP/TAZ in cell-matrix adhesion-mediated signalling and  
273 mechanotransduction. *Exp. Cell Res.* **343**, 42–53 (2016).
- 274 5. Miralles, F., Posern, G., Zaromytidou, A.-I. & Treisman, R. Actin dynamics control SRF activity  
275 by regulation of its coactivator MAL. *Cell* **113**, 329–342 (2003).

- 276 6. Janmey, P. A., Wells, R. G., Assoian, R. K. & McCulloch, C. A. From tissue mechanics to  
277 transcription factors. *Differentiation* **86**, 112–120 (2013).
- 278 7. Coloff, J. L. *et al.* Differential Glutamate Metabolism in Proliferating and Quiescent Mammary  
279 Epithelial Cells. *Cell Metabolism* **23**, 867–880 (2016).
- 280 8. Bays, J. L., Campbell, H. K., Heidema, C., Sebbagh, M. & DeMali, K. A. Linking E-cadherin  
281 mechanotransduction to cell metabolism through force-mediated activation of AMPK. *Nat. Cell*  
282 *Biol.* **19**, 724–731 (2017).
- 283 9. Romani, P. *et al.* Metabolomics and Lipidomics analyses of MCF10ATk1 cells treated with  
284 ROCK/MLCK inhibitors. *Figshare database* (2018). doi:10.6084/m9.figshare.7338764
- 285 10. Zhao, B. *et al.* Cell detachment activates the Hippo pathway via cytoskeleton reorganization to  
286 induce anoikis. *Genes Dev.* **26**, 54–68 (2012).
- 287 11. Aylon, Y. *et al.* The LATS2 tumor suppressor inhibits SREBP and suppresses hepatic  
288 cholesterol accumulation. *Genes Dev.* (2016). doi:10.1101/gad.274167.115
- 289 12. Shimano, H. & Sato, R. SREBP-regulated lipid metabolism: convergent physiology - divergent  
290 pathophysiology. *Nat Rev Endocrinol* (2017). doi:10.1038/nrendo.2017.91
- 291 13. Brown, M. S., Radhakrishnan, A. & Goldstein, J. L. Retrospective on Cholesterol Homeostasis:  
292 The Central Role of Scap. *Annu. Rev. Biochem.* **87**, annurev-biochem-062917-011852 (2017).
- 293 14. Comerford, S. A. *et al.* Acetate Dependence of Tumors. *Cell* **159**, 1591–1602 (2014).
- 294 15. Hsu, C.-K. *et al.* Caveolin-1 Controls Hyperresponsiveness to Mechanical Stimuli and  
295 Fibrogenesis-Associated RUNX2 Activation in Keloid Fibroblasts. *J. Invest. Dermatol.* (2017).  
296 doi:10.1016/j.jid.2017.05.041
- 297 16. Ogawa, R. Mechanobiology of scarring. *Wound Repair Regen* **19 Suppl 1**, s2–9 (2011).
- 298 17. Aya, R. *et al.* The Shear Wave Velocity on Elastography Correlates with the Clinical Symptoms  
299 and Histopathological Features of Keloids. *Plastic and Reconstructive Surgery Global Open* **3**,  
300 e464 (2015).
- 301 18. Tachi, M. & Iwamori, M. Mass spectrometric characterization of cholesterol esters and wax  
302 esters in epidermis of fetal, adult and keloidal human skin. *Experimental Dermatology* **17**, 318–  
303 323 (2008).
- 304 19. Calvo, F. *et al.* Mechanotransduction and YAP-dependent matrix remodelling is required for the  
305 generation and maintenance of cancer-associated fibroblasts. *Nat. Cell Biol.* **15**, 637–646 (2013).
- 306 20. Liu, F. *et al.* Mechanosignaling through YAP and TAZ drives fibroblast activation and fibrosis.  
307 *Am. J. Physiol. Lung Cell Mol. Physiol.* **308**, L344–57 (2015).
- 308 21. Sun, L.-P., Seemann, J., Goldstein, J. L. & Brown, M. S. Sterol-regulated transport of SREBPs  
309 from endoplasmic reticulum to Golgi: Insig renders sorting signal in Scap inaccessible to COPII  
310 proteins. *Proc. Natl. Acad. Sci. U.S.A.* **104**, 6519–6526 (2007).
- 311 22. Watanabe, K. *et al.* A ROCK inhibitor permits survival of dissociated human embryonic stem  
312 cells. *Nat Biotechnol* **25**, 681–686 (2007).
- 313 23. Ohgushi, M. *et al.* Molecular pathway and cell state responsible for dissociation-induced  
314 apoptosis in human pluripotent stem cells. *Cell Stem Cell* **7**, 225–239 (2010).
- 315 24. Storey, M. K., Byers, D. M., Cook, H. W. & Ridgway, N. D. Cholesterol regulates oxysterol  
316 binding protein (OSBP) phosphorylation and Golgi localization in Chinese hamster ovary cells:  
317 correlation with stimulation of sphingomyelin synthesis by 25-hydroxycholesterol. *Biochem. J.*  
318 **336 ( Pt 1)**, 247–256 (1998).
- 319 25. Mohammadi, A. *et al.* Golgi localization and phosphorylation of oxysterol binding protein in  
320 Niemann-Pick C and U18666A-treated cells. *J. Lipid Res.* **42**, 1062–1071 (2001).
- 321 26. De Matteis, M. A. & Godi, A. Protein-lipid interactions in membrane trafficking at the Golgi  
322 complex. *Biochim. Biophys. Acta* **1666**, 264–274 (2004).
- 323 27. D'Souza-Schorey, C. & Chavrier, P. ARF proteins: roles in membrane traffic and beyond. *Nat.*

- 324 *Rev. Mol. Cell Biol.* **7**, 347–358 (2006).
- 325 28. Walker, A. K. *et al.* A conserved SREBP-1/phosphatidylcholine feedback circuit regulates  
326 lipogenesis in metazoans. *Cell* **147**, 840–852 (2011).
- 327 29. Smulan, L. J. *et al.* Cholesterol-Independent SREBP-1 Maturation Is Linked to ARF1  
328 Inactivation. *CellReports* **16**, 9–18 (2016).
- 329 30. Takashima, K. *et al.* COPI-mediated retrieval of SCAP is crucial for regulating lipogenesis  
330 under basal and sterol-deficient conditions. *J. Cell. Sci.* **128**, 2805–2815 (2015).
- 331 31. Zhang, P. & Reue, K. Lipin proteins and glycerolipid metabolism: Roles at the ER membrane  
332 and beyond. *Biochim. Biophys. Acta* **1859**, 1583–1595 (2017).
- 333 32. Peterson, T. R. *et al.* mTOR Complex 1 Regulates Lipin 1 Localization to Control the SREBP  
334 Pathway. *Cell* **146**, 408–420 (2011).
- 335 33. Fernández-Ulibarri, I. *et al.* Diacylglycerol is required for the formation of COPI vesicles in the  
336 Golgi-to-ER transport pathway. *Mol. Biol. Cell* **18**, 3250–3263 (2007).
- 337 34. Asp, L. *et al.* Early stages of Golgi vesicle and tubule formation require diacylglycerol. *Mol.*  
338 *Biol. Cell* **20**, 780–790 (2009).
- 339 35. Baron, C. L. & Malhotra, V. Role of diacylglycerol in PKD recruitment to the TGN and protein  
340 transport to the plasma membrane. *Science (New York, N.Y.)* **295**, 325–328 (2002).
- 341 36. Antonny, B., Huber, I., Paris, S., Chabre, M. & Cassel, D. Activation of ADP-ribosylation factor  
342 1 GTPase-activating protein by phosphatidylcholine-derived diacylglycerols. *Journal of*  
343 *Biological Chemistry* **272**, 30848–30851 (1997).
- 344 37. Harris, T. E. *et al.* Insulin controls subcellular localization and multisite phosphorylation of the  
345 phosphatidic acid phosphatase, lipin 1. *Journal of Biological Chemistry* **282**, 277–286 (2007).
- 346 38. Péterfy, M., Harris, T. E., Fujita, N. & Reue, K. Insulin-stimulated interaction with 14-3-3  
347 promotes cytoplasmic localization of lipin-1 in adipocytes. *J. Biol. Chem.* **285**, 3857–3864  
348 (2010).
- 349 39. Hausser, A. *et al.* Protein kinase D regulates vesicular transport by phosphorylating and  
350 activating phosphatidylinositol-4 kinase IIIbeta at the Golgi complex. *Nat. Cell Biol.* **7**, 880–886  
351 (2005).
- 352 40. Villani, M. *et al.* Sphingomyelin synthases regulate production of diacylglycerol at the Golgi.  
353 *Biochem. J.* **414**, 31–41 (2008).
- 354 41. Liu, G.-H. & Gerace, L. Sumoylation regulates nuclear localization of lipin-1alpha in neuronal  
355 cells. *PLoS ONE* **4**, e7031 (2009).
- 356 42. Li, T. Y. *et al.* Tip60-mediated lipin 1 acetylation and ER translocation determine triacylglycerol  
357 synthesis rate. *Nat Comms* **9**, 1916 (2018).
- 358 43. Isermann, P. & Lammerding, J. Nuclear Mechanics and Mechanotransduction in Health and  
359 Disease. *Current Biology* **23**, R1113–R1121 (2013).
- 360 44. Coste, B. *et al.* Piezo1 and Piezo2 are essential components of distinct mechanically activated  
361 cation channels. *Science (New York, N.Y.)* **330**, 55–60 (2010).
- 362 45. Egea, G., Lázaro-Diéguez, F. & Vilella, M. Actin dynamics at the Golgi complex in mammalian  
363 cells. *Curr. Opin. Cell Biol.* **18**, 168–178 (2006).
- 364 46. Gurel, P. S., Hatch, A. L. & Higgs, H. N. Connecting the Cytoskeleton to the Endoplasmic  
365 Reticulum and Golgi. *Current Biology* **24**, R660–R672 (2014).
- 366 47. Guet, D. *et al.* Mechanical role of actin dynamics in the rheology of the Golgi complex and in  
367 Golgi-associated trafficking events. *Current biology : CB* **24**, 1700–1711 (2014).
- 368 48. Fu, J. *et al.* Mechanical regulation of cell function with geometrically modulated elastomeric  
369 substrates. *Nat. Methods* **7**, 733–736 (2010).
- 370 49. Sato, T. & Clevers, H. Growing self-organizing mini-guts from a single intestinal stem cell:  
371 mechanism and applications. *Science (New York, N.Y.)* **340**, 1190–1194 (2013).

- 372 50. McFarlane, M. R. *et al.* Scap is required for sterol synthesis and crypt growth in intestinal  
373 mucosa. *J. Lipid Res.* **56**, 1560–1571 (2015).
- 374 51. Katsuda, T. *et al.* Conversion of Terminally Committed Hepatocytes to Culturable Bipotent  
375 Progenitor Cells with Regenerative Capacity. *Cell Stem Cell* **20**, 41–55 (2017).
- 376 52. Creutz, C. E., Eaton, J. M. & Harris, T. E. Assembly of high molecular weight complexes of  
377 lipin on a supported lipid bilayer observed by atomic force microscopy. *Biochemistry* **52**, 5092–  
378 5102 (2013).
- 379 53. Watson, R. T. & Pessin, J. E. Transmembrane domain length determines intracellular membrane  
380 compartment localization of syntaxins 3, 4, and 5. *Am. J. Physiol., Cell Physiol.* **281**, C215–23  
381 (2001).
- 382 54. Misumi, Y., Sohda, M., Tashiro, A., Sato, H. & Ikehara, Y. An essential cytoplasmic domain for  
383 the Golgi localization of coiled-coil proteins with a COOH-terminal membrane anchor. *Journal*  
384 *of Biological Chemistry* **276**, 6867–6873 (2001).
- 385 55. Enzo, E. *et al.* Aerobic glycolysis tunes YAP/TAZ transcriptional activity. *EMBO J.* **34**, 1349–  
386 1370 (2015).
- 387 56. Aragona, M. *et al.* A mechanical checkpoint controls multicellular growth through YAP/TAZ  
388 regulation by actin-processing factors. *Cell* **154**, 1047–1059 (2013).
- 389 57. Santinon, G. *et al.* dNTP metabolism links mechanical cues and YAP/TAZ to cell growth and  
390 oncogene-induced senescence. *EMBO J.* **37**, e97780 (2018).
- 391 58. Irizarry, R. A. *et al.* Exploration, normalization, and summaries of high density oligonucleotide  
392 array probe level data. *Biostatistics* **4**, 249–264 (2003).
- 393 59. Tusher, V. G., Tibshirani, R. & Chu, G. Significance analysis of microarrays applied to the  
394 ionizing radiation response. *Proc. Natl. Acad. Sci. U.S.A.* **98**, 5116–5121 (2001).
- 395 60. Kuleshov, M. V. *et al.* Enrichr: a comprehensive gene set enrichment analysis web server 2016  
396 update. *Nucleic Acids Res.* **44**, W90–7 (2016).
- 397 61. Horton, J. D. *et al.* Combined analysis of oligonucleotide microarray data from transgenic and  
398 knockout mice identifies direct SREBP target genes. *Proc. Natl. Acad. Sci. U.S.A.* **100**, 12027–  
399 12032 (2003).
- 400 62. Porstmann, T. *et al.* PKB/Akt induces transcription of enzymes involved in cholesterol and fatty  
401 acid biosynthesis via activation of SREBP. *Oncogene* **24**, 6465–6481 (2005).
- 402 63. Mandal, K., Asnacios, A., Goud, B. & Manneville, J.-B. Mapping intracellular mechanics on  
403 micropatterned substrates. *Proceedings of the National Academy of Sciences* **113**, E7159–E7168  
404 (2016).
- 405  
406

#### 407 **Acknowledgements**

408 We are grateful to Y. Chen, K. Mori, G. DelSal, B. Viollet and H. Louvel, E. Greotti, A. DeMatteis and  
409 R. Venditti, A. Hausser, R. Rizzuto and D. Vecellio Reane, L. Scorrano and L. Pernas, C. Cheng, E.  
410 Melloni, M. Pende and R. Talha, R. Ogawa, J. Goldstein P. Espenshade and W. Shao for advice and  
411 materials. We are indebted to S. Giulitti for generous help with hydrogels, to M. Pellegrini and I.  
412 Zorzan for help with hPSC cultures, to G. Martello and M. Montagner for thoughtful discussion. This  
413 work was supported by AIRC IG-15307, WCR 15-1192, CARIPARO Eccellenza 2017 and University  
414 of Padua BIRD grants to SD, AIRC ‘Hard ROCK Café Fellowship to GS, UPMC ‘Interface pour le  
415 Vivant’ doctoral program to SM, AIRC Special Program Molecular Clinical Oncology ‘5 per mille’  
416 10016 to SB.

#### 417 **Author contributions**

418

419 PR and IB performed experiments and analyzed data with help from GS and AP; MA and SP and NM  
420 performed metabolic measurements and advised on the interpretation of metabolic data; SM and JBM  
421 performed Golgi micromanipulations; MF and SB performed bioinformatics analyses; SD and PR  
422 planned experiments; SD coordinated and supervised the project, and wrote the paper.

423

424 **Competing Interests**

425 The authors declare no competing or financial interests.

426

427 **Figure legends**

428

429 **Figure 1. Actomyosin contractility and ECM mechanical cues regulate lipid synthesis.**

430 **a**, Principal component analysis of metabolites altered by global metabolomics in MCF10ATk1 human  
431 mammary epithelial cells treated for 6 or 24 hours with 20 $\mu$ M Y27632 ROCK inhibitor and 20 $\mu$ M  
432 ML7 MLCK inhibitor to inhibit actomyosin contractility (hereafter YM, n=6 biologically independent  
433 samples), as compared to vehicle (DMSO, n=4 biologically independent samples). **b**, Volcano plot of  
434 lipid molecules altered in MCF10ATk1 cells treated for 24 hours with YM, as measured by targeted  
435 lipidomics. n=5 biologically independent samples per condition. TG, triacylglycerols; DG,  
436 diacylglycerols; LysoPC, lyso-phosphatidylcholines; Cer, ceramides. **c,d**, TG (**c**) and DG (**d**) levels in  
437 MCF10ATk1 cells treated with YM for 24 hours, as measured by mass spectrometry. Only the five  
438 most abundant species are shown. **e,f**, Fatty acids (**e**, n=5 biologically independent samples per  
439 condition) and cholesterol (**f**, n=9 biologically independent samples per condition) in MCF10ATk1  
440 cells treated with YM, as assayed by standard colorimetric assays. **g**, Filipin staining for cholesterol and  
441 Oil-Red-O staining (ORO) for neutral lipids in MCF10ATk1 cells treated with YM or FM  
442 (Fasudil+ML7). Inhibition of cholesterol and fatty acid synthesis with 10 $\mu$ M Cerivastatin (Ceri) or with  
443 15 $\mu$ M TOFA prevents accumulation. Here and through all figures, image acquisition settings were the  
444 same between controls and experimental samples. Scale bar 5 $\mu$ m. **h**, Accumulation of cholesterol and  
445 neutral lipids in MCF10ATk1 cells upon inhibition of RHO (C3 transferase transfection), non-muscle  
446 myosin II (20 $\mu$ M Blebbistatin) or by plating cells on soft ( $E\approx 0.5$ kPa) fibronectin-coated  
447 polyacrylamide hydrogels, compared to stiff ( $E\approx 15$ kPa) hydrogels. Scale bar 5 $\mu$ m. **i**, Transmission  
448 electron microscope pictures of MCF10ATk1 cells plated on stiff or soft hydrogel, with apparent lipid  
449 droplets (LD) and part of the nucleus (N). Scale bar 1 $\mu$ m. **j,k**, non-transformed human RPE1 (**j**) and  
450 primary mouse 3T3L1 (**k**) cells plated on stiff or soft hydrogels. Scale bar 5 $\mu$ m. The images in panels  
451 **g-k** are representative of at least two independent experiments with similar results; quantifications and  
452 n are provided in Supplementary Table 2. Data are mean and single points; unpaired two-tailed  
453 Student's t-tests.

454

455 **Figure 2. ECM mechanical cues regulate SREBP1/2 target genes.**

456 **a**, Gene list enrichment analysis on probes significantly upregulated (mean fold>1.3  $P<0.05$ ) in  
457 microarrays of MCF10ATk1 cells treated with DMSO or Y27632+ML7 (YM) for 6 hours. The graphs  
458 display the 10 most significantly overrepresented gene sets for each of the indicated databases,  
459 analyzed with Enrichr and ranked according to combined score (x axis). Gene sets related to  
460 cholesterol, lipids and SREBP are highlighted in orange. **b**, Heatmap of SREBP target genes in  
461 microarrays of MCF10ATk1 cells treated as in **a**. Each column is an independent biological sample  
462 (n=3 for each condition); each line corresponds to a single gene probe indicated on the right. Blue and  
463 yellow extremes correspond to raw Z-scores of -2 and +2, respectively. **c**, *LDLR-luciferase* reporter  
464 assay for SREBP activity in MDA231 cells treated with YM or Fasudil+ML7 (FM). Mean expression  
465 in controls was set to 1, and other samples are relative to this (n $\geq 6$  independent biological samples per  
466 condition; unpaired Mann-Whitney tests). **d**, qPCR for established SREBP targets in RPE1 cells treated  
467 for 6 or 24 hours with DMSO, YM or FM (n $\geq 4$  independent biological samples per condition; multiple  
468 unpaired two-tailed Student's t-tests). **e-g**, qPCR for established SREBP targets in MCF10ATk1 (**e**),  
469 RPE1 (**f**) or 3T3L1 (**g**) cells plated on stiff ( $E\approx 15$ kPa) or soft ( $E\approx 0.5$ kPa) ECM-coated hydrogels for 24  
470 hours (n $\geq 4$  independent biological samples per condition; multiple unpaired two-tailed Student's t-  
471 tests). In **d-g** data are relative to *GAPDH* levels; mean expression in controls (DMSO or stiff) were set  
472 to 1, and all other samples are relative to this. Data are mean and single points.

473

474 **Figure 3. ECM mechanical cues regulate lipid synthesis by controlling SREBP1/2 activation.**  
475 **a**, qPCR analysis in MCF10ATk1 cells 48 hours after transfection with control siRNA (siCo.) or four  
476 independent mixes of siRNAs targeting *SREBF1* and *SREBF2* mRNAs (siSREBP A to D). **b**, qPCR  
477 analysis of established SREBP1/2 targets in MCF10ATk1 transfected as in **a** and treated with DMSO  
478 or YM for 24 hours. In **a** and **b** mRNA expression data are relative to *GAPDH* levels; mean expression  
479 levels in controls was set to 1, and all other samples are expressed relative to this ( $n \geq 4$  independent  
480 biological samples per condition; unpaired Mann-Whitney tests). **c**, Cholesterol accumulation in  
481 MCF10ATk1 cells transfected with SREBP1/2 siRNA (siSREBP mixes A and B) and plated on soft  
482 hydrogels. Scale bar 5 $\mu$ m. Quantification and n is provided in Supplementary Table 2. **d**,  
483 Immunofluorescence for endogenous SREBP2 in MCF10ATk1 cells with inhibited ROCK/MLCK  
484 (YM), RHO (C3 plasmid transfection), MyosinII (Blebbistatin 10 $\mu$ M), or plated on soft hydrogels for 6  
485 hours. Cell contour in the YM 2h panel (dotted line) helps visualizing SREBP2 concentration at the  
486 Golgi apparatus. Scale bar 10 $\mu$ m.  $n > 50$  cells per condition. **e**, Western blotting for the mature form of  
487 endogenous SREBP1 and SREBP2 in MCF10ATk1 cells treated 4 hours with YM or FM. TEAD1 is a  
488 loading control for nuclear extracts. See also Supplementary Fig. 8. **f**, Immunofluorescence for  
489 endogenous SREBP2 in MCF10ATk1 cells treated 4 hours with YM in the presence of 100 $\mu$ g/ml  
490 cycloheximide (CHX). Scale bar 10 $\mu$ m.  $n > 50$  cells per condition. **g**, Western blotting on total extracts  
491 of MCF10ATk1 cells untreated (-), treated for 3 hours with 2 $\mu$ g/ml puromycin alone (puro) or with  
492 puromycin and 100 $\mu$ g/ml cycloheximide (CHX). Incorporation of the puromycin aminoacid analog  
493 into nascent proteins is used as control for efficient inhibition of protein synthesis. See also  
494 Supplementary Fig. 8. **h**, *LDLR-luciferase* in MDA231 cells. YM and FM activate endogenous  
495 SREBP, but have no additive effects in cells depleted of SREBP1/2 (siSREBP) and expressing a  
496 siRNA-insensitive, cleaved mature SREBP2 cDNA (caSREBP2). Mean expression in controls was set  
497 to 1, and other samples are relative to this ( $n \geq 4$  independent biological samples per condition; unpaired  
498 Mann-Whitney tests). **i**, Heatmap of SREBP and YAP target levels in  $n = 7$  patient-matched soft normal  
499 skin vs. stiff keloid tissue. Each column represents  $-\log_2(\text{keloid/skin})$  values for a single patient; each  
500 line is a single gene probe; genes ranked according to expression in patient #1. Selected gene names are  
501 indicated on the right; only the 60 most up- or downregulated genes ( $P < 0.05$ ) are included. All n values  
502 are pooled between independent experiments. The images in **c-g** are representative of at least two  
503 independent experiments with similar results. Data are mean and single points.  
504

505 **Figure 4. ECM mechanical cues regulate SCAP accumulation to the Golgi apparatus.**  
506 **a**, Co-localization of transfected MYC-tagged SCAP with a Golgi marker (GM130) in MCF10ATk1  
507 cells cultured 6 hours on soft hydrogels ( $E \approx 0.5$ kPa), treated 6 hours with Y27632+ML7 (YM) or  
508 transfected with the C3 RHO inhibitor. Scale bar 10 $\mu$ m.  $n > 50$  cells per condition. **b**, Co-localization of  
509 transfected MYC-SCAP with a Golgi marker (GFP-Rab6) in RPE1 cells treated 6 hours with YM.  
510 Scale bar 10 $\mu$ m.  $n > 50$  cells per condition. **c**, *LDLR-luciferase* in MDA231 cells transfected with  
511 control siRNA (siCo.), with two independent SCAP siRNA (siSCAP A and B), or treated with 30 $\mu$ M  
512 25-hydroxycholesterol (25OHC). **d**, *LDLR-luciferase* in MDA231 cells treated with the site-1 protease  
513 (S1P) inhibitor PF429242 (10 $\mu$ M). **e**, *LDLR-luciferase* in MDA231 cells transfected the C3 RHO  
514 inhibitor and treated as in **c** and **d**. In panels **c-e**,  $n \geq 4$  independent biological samples per condition;  
515 mean expression in controls were set to 1, and all other samples are relative to this; data are mean and  
516 single points; unpaired Mann-Whitney tests. **f**, Human Pluripotent Stem Cells (hPSC) were dissociated  
517 and plated as single cells in the absence (DMSO) or presence of 10 $\mu$ M Y27632, without or with titrated  
518 doses of Cerivastatin (Ceri 25nM) and TOFA (75nM) for 24 hours, released in medium without  
519 inhibitors for 4 days, and stained for alkaline phosphatase to visualize self-renewing colonies. Lower  
520 panels: similar treatment on already-established colonies. Higher doses of Ceri/TOFA (10 $\mu$ M and

521 15 $\mu$ M) inhibit also established colonies. **g**, hPSC plated as in **f** and treated with 1,25 $\mu$ M 25-  
522 hydroxycholesterol. **h**, hPSC transfected with the indicated siRNAs and plated as single cells. The  
523 images in **f-h** are representative of at least two independent experiments with similar results;  
524 quantifications and n are provided in Supplementary Table 2. All n values are pooled between  
525 independent experiments.  
526

### 527 **Figure 5. ECM mechanical cues regulate Lipin-1/ARF1 signaling.**

528 **a,b**, qPCR for SREBP target genes in MCF10ATk1 cells treated with DMSO or with 100 $\mu$ M  
529 Propranolol (Propra) to inhibit Lipin-1 phosphatidate phosphatase activity (**a**), or transfected with  
530 control (siCo.) and Lipin-1 siRNA (siLipin-1) (**b**). Data are relative to *GAPDH* levels; mean expression  
531 in controls was set to 1, and all other samples are relative to this (n $\geq$ 4 independent biological samples  
532 per condition; multiple unpaired Student's t-tests). **c**, *LDLR-luciferase* in MDA231 cells transfected  
533 with the indicated siRNA and treated with 100 $\mu$ M Propranolol (Propra). Mean expression in the control  
534 was set to 1, and all other samples are relative to this (n $\geq$ 4 independent biological samples per  
535 condition; unpaired Mann-Whitney tests). **d**, Immunofluorescence for endogenous SREBP2 in  
536 MCF10ATk1 cells treated with Propranolol, transfected with Lipin-1 or COPI siRNA, or expressing  
537 dominant-negative ARF1-T31N-GFP (DN ARF1). Scale bar 10 $\mu$ m. n>50 cells per condition. **e**, Co-  
538 localization of transfected MYC-SCAP with the GFP-Rab6 Golgi marker in RPE1 cells treated 6 hours  
539 with Propranolol, in cells transfected with control (siCo.), Lipin-1 or COPI siRNAs, or expressing  
540 dominant-negative ARF1-T31N (DN ARF1). Scale bar 10 $\mu$ m. n>50 cells per condition. **f**, Lipid  
541 staining in MCF10ATk1 cells treated for 24 hours with YM, with 100 $\mu$ M Propranolol, or transfected  
542 with Lipin-1 siRNA. Scale bar 5 $\mu$ m. Quantifications and n are provided in Supplementary Table 2. **g**,  
543 Western blotting for Lipin-1 levels in microsomal fractions from MCF10ATk1 cells treated 3 hours  
544 with DMSO or Y27632+ML7 (YM). Calreticulin (ER marker) and GM130 (Golgi marker) are loading  
545 controls. See also Supplementary Fig. 8. **h**, Co-localization of transfected GFP-PKD-KD with the  
546 GM130 Golgi marker in HEK293 cells treated for 30 min with YM, with 100 $\mu$ M Propranolol, or  
547 transfected with control (siCo.) and Lipin-1 siRNAs. Scale bar 10 $\mu$ m. Mean Pearson's correlation  
548 coefficient and SD for co-localization is indicated above each panel (n $\geq$ 10 cells were measured for  
549 each condition). **i**, GST-GGA3-PBD pulldown for GTP-bound active ARF1 (GTP-Arf1) and western  
550 blotting for ARF1 in the total extracts (Total Arf1). Cells were treated 3 hours with DMSO or YM. See  
551 also Supplementary Fig. 8. **j**, Co-localization of endogenous ARF1 with a Golgi marker (GM130) in  
552 MCF10ATk1 cells treated 6 hours with YM or Propranolol. Scale bar 10 $\mu$ m. Mean Pearson's  
553 correlation coefficient and SD for co-localization is indicated above each panel (n $\geq$ 10 cells were  
554 measured for each condition). The images in **d-j** are representative of at least two independent  
555 experiments with similar results. All n values are pooled between independent experiments. Data are  
556 mean and single points.  
557

### 558 **Figure 6. Actomyosin contractility regulates SREBP through Lipin-1.**

559 **a**, Western blotting for transfected FLAG-tagged Lipin-1 in HEK293 cells treated with DMSO or YM  
560 for 6 hours. The 17S/A mutant is not phosphorylated and migrates faster than WT Lipin-1. GAPDH  
561 serves as loading control. See also Supplementary Fig. 8. **b**, Immunofluorescence for transfected  
562 FLAG-Lipin-1 in MCF10ATk1 cells treated 6 hours with YM, Blebbistatin, or plated on a soft  
563 hydrogel. Scale bar 10 $\mu$ m. n>50 cells per condition. **c**, Immunofluorescence for transfected wild-type  
564 (WT) or 17S/A FLAG-tagged Lipin-1 isoforms in RPE1 cells, treated with DMSO, YM or Torin1  
565 (500nM) for 6 hours. Fusion with the membrane-localization domain of Syntaxin5 tethers MB-Lipin-1  
566 to cytoplasmic membranes. Scale bar 10 $\mu$ m. n>50 cells per condition. Similar results were obtained

567 with MB\*-Lipin-1 (used in **d**) and in other cell lines. **d**, *LDLR-luciferase* (top) and *FASN-luciferase*  
568 (bottom) assays in MDA231 cells treated with the ROCK/MLCK inhibitor FM and transfected with  
569 wild-type (WT), membrane-tethered (MB and MB\*) or 17S/A Lipin-1 isoforms. **e**, *LDLR-luciferase*  
570 (top) and *FASN-luciferase* (bottom) assays in MDA231 cells transfected with the C3 RHO inhibitor  
571 without or with membrane-tethered (MB) Lipin-1. In **d** and **e**, mean expression in the control was set to  
572 1, and all other samples are relative to this;  $n \geq 4$  independent biological samples per condition; unpaired  
573 Mann-Whitney tests. **f**, MDA231 cells were transfected with WT-Lipin-1 or MB-Lipin-1 together with  
574 mCherry (RFP), treated with YM, and stained for cholesterol.  $n > 30$  cells per condition. Graph: cells  
575 were scored positive (+ve) for Filipin based on the presence/absence of cytoplasmic cholesterol  
576 accumulation. The images in **a**, **b**, **c** and **f** are representative of at least two independent experiments  
577 with similar results. All n values are pooled between independent experiments. Data are mean and  
578 single points.  
579

580 **Figure 7. The Golgi apparatus responds to extracellular physical cues and intracellular force**  
581 **application.**

582 **a**, Co-localization of transfected MYC- SCAP with the GFP-Rab6 Golgi marker in RPE1 cells freely  
583 spreading on fibronectin-coated glass (Large) or plated on micropatterned fibronectin islands  
584 restraining cell area and inducing low F-actin tension (Small,  $960 \mu\text{m}^2$  or  $490 \mu\text{m}^2$ ). Scale bar  $10 \mu\text{m}$ .  
585  $n > 30$  cells per condition. **b**, Golgi rheology was measured in RPE1 cells plated as in **a**. GFP-Rab6-  
586 positive Golgi membranes were pushed towards a cytoplasmic bead immobilized by an optical trap in a  
587 series of five  $0.5 \mu\text{m}$  steps in 1 min (see Supplementary Fig. **7a** and Methods). The graph shows the  
588 averaged displacements of the bead during the first step (see Supplementary Fig. **7b** for the complete  
589 graph). Green line: large unconfined cells, conditions of high tension ( $n = 39$  cells). The Golgi  
590 microenvironment displays a visco-elastic behavior as the bead is first maximally displaced (Bead Step  
591 Amplitude), and then slowly relaxes back due to attraction from the optical trap. Orange and Red lines:  
592 micropatterned small ECM ( $n = 28, 21$  cells). Gray shadows: s.e.m. error bars. A smaller displacement  
593 and a faster relaxation of the bead indicate a lower rigidity of the Golgi apparatus. **c**, The Rigidity  
594 Index (RI) measures the friction opposed by the Golgi microenvironment on the bead, with lower  
595 values indicating a softer microenvironment. The Bead Step Amplitude corresponds to the average  
596 displacement of the bead after each step, with lower values indicating a softer microenvironment. The  
597 Ejection Frequency measures the relative frequency of experiments in which the bead falls off the  
598 optical trap, which is increased with the resisting friction forces applied on the bead by the Golgi. **d**,  
599 Time-lapse confocal images of a representative RPE1 cell transfected with the GFP-PKD-KD  
600 diacylglycerol sensor and with a Golgi-localized mCherry. A  $2 \mu\text{m}$ -diameter cytoplasmic bead (yellow  
601 dotted line) was immobilized by an optical trap in the proximity of the Golgi apparatus ( $t = 0$ ) and then  
602 pushed every 5 min. towards the Golgi (white arrow: direction of the compressive constraint). **e**,  
603 Normalized intensity of the PKD-KD signal before and after application of force ( $n = 19$  cells). In the  
604 control the bead was moved away from the Golgi towards the cytoplasm ( $n = 18$  cells). The images in **a**  
605 and **d** are representative of at least two independent experiments with similar results. All n values are  
606 pooled between independent experiments. Data are mean and s.e.m.; two-tailed unpaired Student's t-  
607 tests.  
608

## 1 **Methods**

2  
3 **Reagents.** Plasmids encoding for SCAP-MYC, HA-S1P, HA-S2P were from Y. Chen (SIBS  
4 Shanghai), Perilipin3-RFP from L. Scorrano (UniPd), kinase-dead GFP-PKD1-K612W from A.  
5 Hausser (UniStuttgart), ARF1-T31N-GFP from A. DeMatteis (TIGEM Naples), KDEL-mCherry from  
6 E. Greotti (UniPd), GFP-OSBP from N. Ridgway (UniGlasgow). Addgene plasmids: FASN-lux #8890;  
7 LDLR-lux #14940; 8XGTIIC-lux #34615; NF2 #19701; CMV-Luc2P\_ARE #62857; constitutive-  
8 active FLAG-SREBP2 #26807; FLAG-Lipin-1 WT #32005 and 17S/A #32007; mCherry-  
9 Golgi(B4GALT1) #55052. Full length SREBP1 and SREBP2 were subcloned from Addgene plasmids  
10 #32017 and #32018. ER/Golgi membrane-tethered Lipin-1 isoforms were obtained by in-frame fusion  
11 of the Syntaxin5 delta220 or TMD fragments<sup>53,54</sup> to FLAG-Lipin-1 WT and have been deposited as  
12 Addgene plasmids #120277 and #120278. SUMOylation (K616/646A) and acetylation (K476/646A)  
13 FLAG-Lipin-1 mutants were obtained by targeted mutagenesis. All plasmids were sequence-verified  
14 before use and transfected as endotoxin-free maxi preps.

15 Small molecule inhibitors were: Y27632 (Axon 1683, 20 microM, 10 microM on hPSC);  
16 Fasudil/HA1077 (SantaCruzBiotechnology sc358231, 20 microM); ML7 (Sigma I2764, 20 microM);  
17 Blebbistatin (Sigma B0560, 20 microM); Propranolol (Sigma P0884, 100 microM); Cycloheximide  
18 (Sigma C1988, 100 microg/ml); TOFA (Sigma T6575, 15 microM, 75 nanoM on hPSC); Cerivastatin  
19 (Sigma SML0005, 10 microM, 25 nanoM on hPSC); 25-hydroxy-cholesterol (Sigma SML2042, 30  
20 microM, 1.25 microM on hPSC); U18666A (SantaCruzBioTechnology sc203306, 3 microM);  
21 PF429242 (Sigma SML0667, 10 microM); Z-VAD-FMK (Sigma V116, 30 microM); Torin1 (Axon  
22 1833, 500 nanoM); MG132 (Sigma C2211, 10 microM); MG115 (Sigma C6706, 10 microM).

23 siRNAs were selected among FlexiTube GeneSolution 4 siRNA sets (Qiagen) and reordered  
24 after validation as dTdT-overhanging 19nt RNA duplexes (Thermo). siRNA sequences: SREBF1a  
25 CGGAGAAGCUGCCUAUCAA; SREBF1b GCGCACUGCUGUCCACAAA; SREBF1c  
26 GCGCACUGCUGUCCACAAA; SREBF1d ACAGCAACCAGAACTCAA; SREBF2a  
27 GCAGUGUCCUGUCAUUCGA; SREBF2b GCAAUUUGUCAGUAAUCAA; SREBF2c  
28 GGCCAUUGAUUACAUCAA; SREBF2d CGAUAUUCGUCCUCCAUCA; SCAPa  
29 GGAAGAUCGACAUGGUCAA; SCAPb GGCCGACGCUCUUCAGCUA; LPIN1  
30 GUUCGGAUACCUUCAGUAA; YAP CUGGUCAGAGAUACUUCUU; TAZ  
31 AGGUACUCCUCAAUCACA; AMPKa1/2 mixes a and b see Ref.<sup>55</sup>; COPIa  
32 GAUUUACCGAGGAGCAUUA; COPIb GGAUCGCUUGAUAGAAUUA; AllStars Negative  
33 Control (Qiagen) sequence not available – proprietary information.

34  
35 **Cell cultures.** MCF10A, MCF10ATk1 MCF10ATk1 pBABE mTAZ 4SA were cultured in  
36 DMEM/F12 5%HS Insulin (Sigma) Cholera Toxin (Sigma) hEGF (Peprotech) and Hydrocortisone  
37 (Sigma). GFP-Rab6 and parental RPE1 in DMEM/F12 10%FBS (neomycin for GFP-Rab6). MDA-  
38 MB-231 in DMEM/F12 10%FBS. HEK293 in DMEM 10%FBS. WI-38 in MEM 10%FBS 5% oxygen.  
39 3T3-L1 in DMEM 10%FBS 5% oxygen. H9 hPSC in E8 medium (DMEM/F12, NaHCO<sub>3</sub>, Insulin,  
40 Selenium, Transferrin, L-ascorbic acid, FGF2, TGFb1) 5% oxygen. WT and AMPKa1/2-/- MEFs in  
41 DMEM 20%FBS. Glutamine was freshly added to a final concentration of 20mM to all media. General  
42 media, serum and supplements were from Thermo. Cytokines from Sigma and Peprotech. All cell lines  
43 were routinely tested with ATCC Universal Mycoplasma Detection kit to exclude contaminations.  
44 Cells for immunofluorescence in a stiff microenvironment were plated on fibronectin-coated glass  
45 coverslips. Stiff (E≈15KPa) and soft (E≈0.5KPa) fibronectin-coated polyacrylamide hydrogels were  
46 assembled in-house by standard protocols. Annular-shaped micropatterns (25 or 35μm diameter, 5μm  
47 line thickness) were printed on PEG-coated glass coverslips by deep UV photolithography and coated  
48 with 50μg/ml fibronectin supplemented with 20μg/ml Alexa647-fibrinogen (Sigma). hPSC were

49 dissociated with Tryple (Thermo) and plated as single cells (2500 cells/2cm<sup>2</sup> well) in the presence or  
50 absence of the indicated small molecules for 24 hours; medium was then changed and cells were left  
51 growing for 4-5 days, until the appearance of macroscopic colonies. Treatment of colonies was done on  
52 colonies grown from single cells as above, and then treating for 24 hours. Cell transfections were  
53 carried out with Transit-LT1 (MirusBio) or with Lipofectamine RNAi-MAX (Thermo).

54  
55 **Antibodies, immunofluorescence and stains.** See Supplementary Table 1 for catalog numbers,  
56 dilutions and validations. For the SREBP2 antibodies, independent lots were used with consistent  
57 results. Immunofluorescence was performed as in<sup>56</sup> with minor modifications: 10min 1.5mg/ml glycine  
58 in PBS before permeabilization to reduce background; blocking in 1-2% BSA. Images were acquired  
59 sequentially with a Zeiss LSN700 or a Leica SP5 confocal microscope equipped with a CCD camera  
60 using ZEN 2 or Leica LAS AF softwares. Typical acquisition settings for IF were: image size  
61 1024x1024 pixels; acquisition mode xyz; pixel size 0.15µm; image depth 8 bits; acquisition speed 5/10,  
62 with average 2; Plan-Apochromat 63x/1.40 oil DIC M27 objective. For multichannel acquisitions, we  
63 used a main beam splitter 405/488/555/639. Raw images (saved in .czi or .lif formats) were opened in  
64 ImageJ and saved in exportable formats. If needed, colors were changed (e.g. red to green) with  
65 Photoshop CC.

66 Oil Red-O staining (Sigma) was carried out after fixation, in 60% v/v isopropanol/water. C11-  
67 Bodipy581/591 (Thermo) were incubated 15min with cells before FACS analysis. Filipin staining was  
68 acquired using a UV filter set (340/380nm excitation, 40nm dichroic, 430nm long pass filter) by  
69 prefocusing cells based on TOTO3 nuclear counterstain (633/647nm) and then acquiring the UV  
70 channel without prior observation to avoid photobleaching. Typical acquisition settings for Filipin  
71 were: image size 1024x1024 pixels; acquisition mode xyz; pixel size 0.15µm; image depth 8 bits;  
72 acquisition speed 5/10, with average 2; Plan-Apochromat 63x/1.40 oil DIC M27 objective. Pictures  
73 were always taken by using the same acquisition conditions between all different experimental  
74 samples; panels are representative pictures based on at least two independent experiments.

75 Quantifications and n are provided in Supplementary Table 2.

76 Alkaline phosphatase staining was Leukocyte AP kit (Sigma). Panels shown are representative  
77 pictures of one biological replicate of one experiment; each experiment was repeated three times  
78 independently. Quantifications and n are provided in Supplementary Table 2.

79  
80 **Cell fractionation, western blotting and pulldown.** Nuclear extracts and microsomes were obtained  
81 by resuspending cells in lysis buffer (250mM Sucrose, 10mM Triethanolamine pH=7.4, 10mM  
82 AceticAcid, 1mM EDTA, 10mM KCl) and passing cells 8 times (i.e. complete lysis at the microscope)  
83 through an Isobiotec Cell Homogenizer with a 6micron clearance sphere. Lysates were centrifuged at  
84 800rcf to isolate nuclei, and then at 100.000rcf to isolate microsomes. Western blotting was performed  
85 as in Ref<sup>57</sup>; in Fig. 3e and Supplementary Fig. 3h cells were incubated with 10microM MG132/MG115  
86 proteasome inhibitors during treatment to prevent degradation of cleaved SREBPs. Active GTP-bound  
87 ARF1 pulldown was performed with a commercial kit following the manufacturer's intructions  
88 (Cytoskeleton Inc. BK032).

89  
90 **Gene expression studies.** Luciferase assays were performed in MDA-MB-231 cells as in  
91 Ref.<sup>55</sup>. For qPCR, total RNA was isolated using commercial kits with DNase treatment (Qiagen,  
92 Norgen). cDNA synthesis was carried out with M-MLV Reverse Trascriptase (Thermo) and oligo-dT  
93 primers. qPCR reactions were assembled with FastStart SYBR Green Master Mix (Roche) and run on a  
94 QuantStudio6 thermal cycler (Thermo). Gene expression levels for each biological sample was  
95 quantified as the mean between three technical replicates; *GAPDH* expression levels were used to  
96 normalize gene expression between samples, based on the  $2^{-\Delta\Delta Ct}$  method.

97 Sequences of primers: *ACSS2* For GTT GAC TCC CCT TCC TGG TG, Rev CTT CCA ACT  
98 CTT CCC CGG AC; *CTGF* AGG AGT GGG TGT GTG ACG Rev ACC AGG CAG TTG GCT CTA  
99 ATC; *DHCR7* For CCG CCC AGC TCT ATA CCT TG, Rev ACT TGT TCA CAA CCC CTG CA;  
100 *FASN* For GGA GGA GTG TAA ACA GCG CT, Rev TTG GCA AAC ACA CCC TCC TT; *HMGCR*  
101 For TGC AGC AAA CAT TGT CAC CG, Rev CAC CAC CCA CCG TTC CTA TC; *HMGCS1* For  
102 ACA CAA GAT GCT ACA CCG GG, Rev ATG GGT GTC CTC TCT GAG CT; *LDLR* For AAG  
103 GAC ACA GCA CAC AAC CA, Rev AAA GGA AGA CGA GGA GCA CG; *LPN1* For ACA TGG  
104 ATC CTG AAG TGG CG, Rev GAG ATG GCG ATG GAA GGG AG; *SQLE* For AGG CGC AGA  
105 AAA GGA ACC AA, Rev GCC AGC TCC CAC GAT GAT AA; *SCD* For CCA CTT GCT GCA  
106 GGA CGA TA, Rev CCA AGT AGA GGG GCA TCG TC; *SREBF1* For CGT TTC TTC GTG GAT  
107 GGG GA, Rev CCC GGA ATA GCT GAG TCA CC; *SREBF2* For GGG CTG GTT TGA CTG GAT  
108 GA, Rev AGA TCT GCC TGT TTC CGG TG; *SCAP* For CAG CAG CAA CAC AGT GAC CT, Rev  
109 TAT GGT CTT GGC TCC CTG TC; *GAPDH* For CTC CTG CAC CAC CAA CTG CT, Rev GGG  
110 CCA TCC ACA GTC TTC TG; *COPI* For AGT ACA GCC TGA TGA CCC CA, Rev TGC TGC CTC  
111 TTT CCT CTG TG; *AMPK $\alpha$ 1* For CTT GCC AAA GGA GTG ATT CAG ATG C, Rev AGG TCA  
112 ACA GGA GAA GAG TCA AGT GT; *AMPK $\alpha$ 2* For AGC GTT CCT GTT CTG CTG CT, Rev TCC  
113 ATG GTG TGA CTG CCC AG.

114 Microarray probe synthesis, hybridization and detection were performed at CMB Trieste on  
115 HumanHT-12 v4 Expression BeadChips with an Illumina Hiscan system. Data analyses were  
116 performed in R (version 3.0.2) using Bioconductor libraries (BioC 2.13) and R statistical packages.  
117 Probe level signals were converted to expression values using robust multi-array average procedure  
118 RMA<sup>58</sup> of Bioconductor Affymetrix package. Differentially expressed genes were identified using  
119 Significance Analysis of Microarray (SAM) algorithm coded in the same R package<sup>59</sup>. In SAM, we  
120 estimated the percentage of false-positive predictions (i.e., false discovery rate, FDR) with 100  
121 permutations. Genes activated or inhibited upon YM treatment and used for Gene List Enrichment  
122 Analysis were filtered based on  $P$ -value<0.05 and fold change>1.3. Gene List Enrichment Analysis  
123 was performed with Enrichr<sup>60</sup>. SREBP target genes were defined based on Ref.<sup>61,62</sup>.

124  
125 **Metabolomics and metabolic analyses.** Large-scale metabolic analysis (global metabolomics) and  
126 Principal Component Analysis of the results was carried out by Metabolon Inc. Mechanosensitive  
127 MCF10Tk1 cells<sup>56</sup> were washed once in warm 1XPBS, and metabolites were extracted 5 min at RT on  
128 15cm plates with 80% v/v Methanol/Water extraction buffer with internal standards. We harvested  
129 cells on plate to specifically avoid alteration of actin tension and of metabolism due to cell detachment.  
130 Metabolites were normalized to protein content. This analysis did not focus on triglyceride content.  
131 Clustering of selected lipid metabolites (fold change>2.5; p-value<0.05) shown in Supplementary Fig.  
132 **1e** was carried out with Heatmapper.

133 Targeted lipidomic analysis was carried out on MCF10Tk1 cells lysed in 1:1 v/v  
134 MeOH/Acetonitrile extraction buffer by tissue lyser and spun at 20,000g for 5 min at 4°C. Supernatant  
135 were then passed through a regenerated cellulose filter, dried and resuspended in 100 $\mu$ l of MeOH.

136 For the quantification of the different phospholipid species the liquid chromatography tandem  
137 mass spectrometry LC-MS/MS analysis was performed on API-4000 triple quadrupole mass  
138 spectrometer (AB Sciex) coupled with a HPLC system (Agilent) and CTC PAL HTS autosampler  
139 (PAL System). The identity of the different phospholipid families was confirmed using pure standards,  
140 namely one for each family. Methanolic extracts were analyzed by a 5 minutes run in both positive and  
141 negative ion mode with a 275 multiple reaction monitoring (MRM) transitions in positive mode and 92  
142 MRM transitions in negative mode. Quantification of different phospholipids in positive ion mode was  
143 performed using a Synergi 4 $\mu$  Hydro-RP (50mm x 2.0mm, 4 $\mu$ m; Phenomenex) and in negative ion  
144 mode using Cyano-phase LUNA column (50mm x 4.6mm, 5 $\mu$ m; Phenomenex). The mobile phase for

145 positive ion mode was 0.1 % formic acid in MeOH and 5 mM ammonium acetate pH 7 in MeOH for  
146 negative ion mode both with a with a flow rate of 500 $\mu$ l/min. MultiQuant™ software version 3.0.2 was  
147 used for data analysis and peak review of chromatograms. Semi-quantitative evaluation of different  
148 phospholipids was performed based on external standards, then data were normalized on protein  
149 content assessed by BCA method.

150 For the quantification of the different diacylglycerol and triacylglycerol species the liquid  
151 chromatography tandem mass spectrometry LC-MS/MS analysis was performed on API-4000 triple  
152 quadrupole mass spectrometer (AB Sciex) coupled with a HPLC system (Agilent) and CTC PAL HTS  
153 autosampler (PAL System). Methanolic extracts were dried under nitrogen and resuspended in 100 $\mu$ l of  
154 65% Acetonitrile/30% isopropanol/5% water. Samples were then analyzed by a 10 minutes run in  
155 positive ion mode with a 92 multiple reaction monitoring (MRM) transitions. Quantification of  
156 different diacylglycerols and triacylglycerols was performed using a XBridge™ C-18 (100mm x  
157 2.1mm, 3.5 $\mu$ m; Waters). Column temperature was set at 55°C. The mobile phases were phase A: 40%  
158 acetonitrile, 0.1 % formic acid and 10 mM ammonium acetate in water; phase B: isopropanol 90%,  
159 acetonitrile 10%, 0.1 % formic acid and 10 mM ammonium acetate. T<sub>0</sub>: 55%A; T<sub>2min</sub>: 55%A; T<sub>4min</sub>:  
160 3%A; T<sub>7min</sub>: 3%A; T<sub>7.1min</sub>: 55%A; T<sub>10min</sub>: 55%A; with a flow rate of 260 $\mu$ l/min. MultiQuant™ software  
161 version 3.0.2 was used for data analysis and peak review of chromatograms. Semi-quantitative  
162 evaluation of different diacylglycerols and triacylglycerols was performed based on external standards,  
163 then data were normalized on protein content assessed by BCA method.

164 For isotopolog analysis, cells were exposed to 2.5mM [<sup>13</sup>C<sub>2</sub>]acetate (Sigma 282014) for 24h.  
165 After removing media, cells were washed in ice-cold PBS. Lipid extraction was performed by adding  
166 500 $\mu$ l of MeOH/ACN (1:1 v/v), and then 2.5ml of chloroform-MeOH (1:1, v/v). Total FAs were  
167 obtained by acid hydrolysis adding 1.25ml of HCl 1M and 1.25ml of MeOH. After leaving samples 1h  
168 in agitation at 210 rpm, 2.5ml of chloroform-water (1:1, v/v) were added to the mixture and the lower  
169 organic phase was collected, split, transferred into tubes, and dried under nitrogen flow. The residue  
170 was resuspended in MeOH/H<sub>2</sub>O (1:1, v/v) and used for total FA analysis. Sample were analyzed by and  
171 API 4000 mass spectrometer (AB Sciex) coupled with a HPLC system (Agilent) and CTC PAL HTS  
172 autosampler (PAL System). The gradient (flow rate 0.5 ml/min) was as follows: T0: 20% A, T20: 1%  
173 A, T25: 1% A, T25.1: 20% A, T30: 20% A, where A: acetic acid 15mM and N-ethylisopropylamine  
174 10mM in H<sub>2</sub>O:MeOH 97:3 and B: MeOH. The Hypersil GOLD™ column (C8 100mm x 3mm, 3 $\mu$ m;  
175 Thermo-Scientific) was maintained at 40°C for all the analysis.

176 For the quantification of free and total fatty acids and cholesterol levels, we used an aliquot of  
177 extracts described above and commercial kits (Sigma MAK044 and MAK043) following the  
178 instructions.

179  
180 **Intracellular optical micromanipulation, microrheological measurements and analysis.** The set-up  
181 combining optical trapping and confocal imaging was described previously<sup>47</sup>. Briefly, red fluorescent  
182 580/605nm 2 $\mu$ m diameter latex beads (Thermo F88265) were endocytosed overnight in RPE1 cells  
183 stably expressing the Golgi marker GFP-Rab6. The incubation time and bead concentration were  
184 adjusted so that cells typically contained one or two beads before optical micromanipulation. Cells  
185 were plated on 18mm diameter coverslips uniformly coated with fibronectin, or with annular-shaped  
186 adhesive fluorescent micropatterns of different diameters (25 or 35  $\mu$ m), during 6 hours. Non-adherent  
187 cells were washed off by rinsing with culture medium. The coverslip was then mounted in a Ludin  
188 chamber and the culture medium was supplemented with 20mM Hepes prior to the experiment.

189 Force was applied on GFP-positive Golgi membranes by first trapping a bead located close to  
190 the Golgi apparatus and then displacing the microscope stage in order to push the organelle against the  
191 trapped bead. Trapping was not possible on polyacrilamide hydrogels because of the excessive distance

192 between lens and cells in this set-up. The applied force  $F$  was deduced from the bead displacement  
193 relative to the trap center  $\Delta x$  after calibration of the trap stiffness  $k_{\text{trap}}$  using  $F = k_{\text{trap}} \Delta x$  with  
194  $k_{\text{trap}} = 280 \text{ pN}/\mu\text{m}$ . The output power of the infra-red laser at the objective aperture was 150 mW.  
195 Stage displacement was performed using a nanopositioning piezo-stage (Nanobio 200, Mad City Labs)  
196 controlled by the NanoRoute3D software (Mad City Labs). The stage displacement consisted in five  
197 consecutive  $0.5\mu\text{m}$  steps with a 10s pause between each step to allow visco-elastic relaxation of the  
198 bead position towards the trap center. The total duration of optical trapping was limited to 1 min for a  
199 given cell to ensure cell viability.

200 To characterize the rigidity of the microenvironment surrounding the bead, we used a  
201 phenomenological analysis of the relaxation curves as in<sup>47,63</sup> to measure three parameters: the  
202 frequency of bead ejection, the bead step amplitude and the rigidity index. Qualitatively, in a low  
203 rigidity microenvironment, friction on the bead is low and the bead does not move much from the trap  
204 center during the step displacement and relaxes rapidly towards the trap center. In a rigid  
205 microenvironment, the bead experiences a high friction and its initial displacement is bigger and closer  
206 to the step displacement ( $0.5\mu\text{m}$ ) and the relaxation is slower. If the force acting on the bead is too  
207 large (typically above  $300\text{-}400\text{pN}$ ), the bead falls off the trap and subsequently follows the  
208 displacement of the stage. We termed such events ‘ejections’ and scored their frequency (defined as the  
209 ratio between the number of experiments in which ejection occurred and the total number of  
210 experiments) and the step at which ejection occurred. The bead step amplitude  $X_b$  corresponds to the  
211 displacement of the bead after a  $0.5\mu\text{m}$  step of the piezo-stage. Values of  $X_b$  close to  $0.5\mu\text{m}$  indicate a  
212 high rigidity of the bead microenvironment. Lower values are indicative of softer microenvironments.  
213 The rigidity index is defined as

$$RI = \frac{\int_{t_i}^{t_i+T} x_b(t) dt}{\int_{t_i}^{t_i+T} x_s(t) dt} = \frac{\int_{t_i}^{t_i+T} x_b(t) dt}{X_s T}$$

214 where  $t_i$  is the time when the  $i^{\text{th}}$   $0.5 \mu\text{m}$  step displacement of the piezo-stage occurs,  $x_b$  and  $x_s$  are  
215 respectively the displacement of the bead relative to the trap center and the displacement of the piezo-  
216 stage,  $X_s = 0.5\mu\text{m}$  is the amplitude of the piezo-stage step and  $T = 10\text{s}$  is the duration of the step. The  
217 rigidity index  $RI$  is a phenomenological parameter which allows us to compare the rigidity of the  
218 microenvironment surrounding the bead in various conditions. The value of  $RI$  falls between 0 (the  
219 microenvironment does not exert any friction on the bead) and 1 (the microenvironment is not  
220 deformable). The values of  $RI$  for each step displacement were averaged.

221 To measure GFP-PKD-KD recruitment upon force application, cells were plated at day 1 in a  
222 12-well plate to reach around 75% confluence on day 2. At day 2, cells were transfected with GFP-  
223 PKD-KD and mCherry-Golgi(B4GALT1) plasmids. At the end of day 2, the cells were incubated with  
224  $2\mu\text{m}$  diameter fluorescent beads overnight. At day 3, cells were transferred to fibronectin-coated  
225 coverslips for the experiment. The evolution of normalized intensity of GFP-PKD-KD in the region of  
226 the Golgi apparatus, visualized by the mCherry-Golgi marker, was monitored after application of a  
227 mechanical constraint exerted by internalized beads trapped with optical tweezers. A bead located near  
228 the Golgi apparatus was selected in a cell expressing GFP-PKD-KD and the mCherry-Golgi marker. A  
229 first image was taken at  $t=0\text{min}$ . The bead was then trapped with the optical tweezers and the  
230 microscope stage manually displaced to bring the Golgi apparatus in contact with the bead and apply a  
231 compressive constraint on the Golgi apparatus during 1 min. The same protocol was repeated every  
232 5min until  $t=30\text{min}$ . The duration of the compressive constraint was reduced to 30s after  $t=10\text{min}$   
233 to avoid cellular damage due to prolonged laser exposure. As a control, the same protocol was used but  
234 the microscope stage was displaced in order to move the bead away from the Golgi apparatus.

235 To quantify the fluorescence intensity of GFP-PKD-KD in each of the seven images taken every  
236 5 minutes, the Golgi apparatus was delimited using the mCherry Golgi marker. The total intensities of  
237 the mCherry Golgi marker ( $I_r$ ) and of GFP-PKD-Kd ( $I_g$ ) were measured as well as the mean intensity  
238 of the background for each channel ( $\langle I_{r \text{ back}} \rangle$  for the mCherry Golgi marker and  $\langle I_{g \text{ back}} \rangle$  for GFP-PKD-  
239 KD) and the area of the Golgi apparatus  $A_{\text{Golgi}}$ . The total intensity of the background in the Golgi  
240 apparatus region for each channel was then estimated by multiplying the mean background intensity by  
241 the Golgi area:

$$I_{r \text{ back}} = A_{\text{Golgi}} \cdot \langle I_{r \text{ back}} \rangle$$
$$I_{g \text{ back}} = A_{\text{Golgi}} \cdot \langle I_{g \text{ back}} \rangle$$

242 The fluorescence intensity of GFP-PKD-KD was normalized by the fluorescence intensity of  
243 the mCherry Golgi marker:

$$I = \frac{I_g - I_{g \text{ back}}}{I_r - I_{r \text{ back}}}$$

244 to account for slight changes in the imaging plane from one image to the next. The relative  
245 temporal variations of the GFP-PKD-KD fluorescence were obtained by normalizing the intensity  $I$   
246 measured from each image taken every 5 minutes by its initial value  $I_0$ :  $I(t) = I/I_0$ .

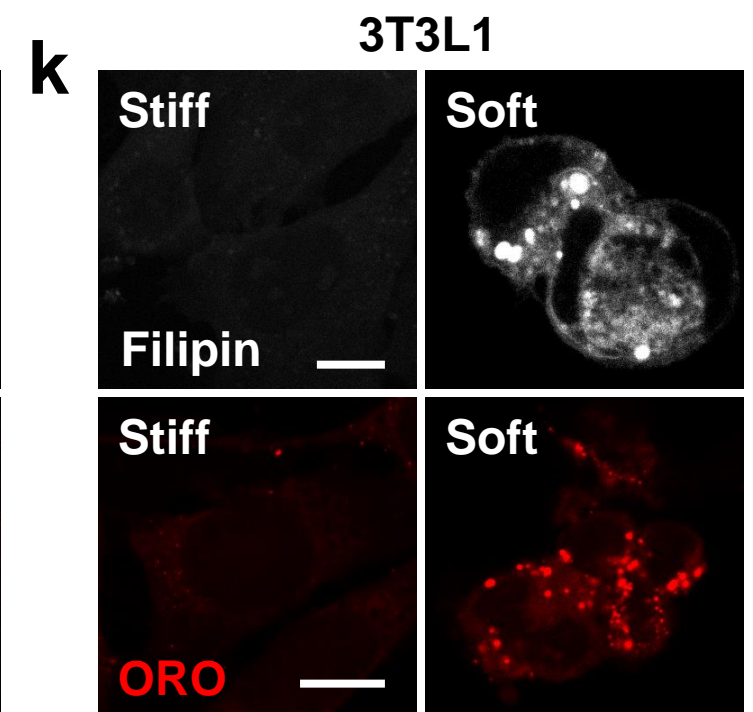
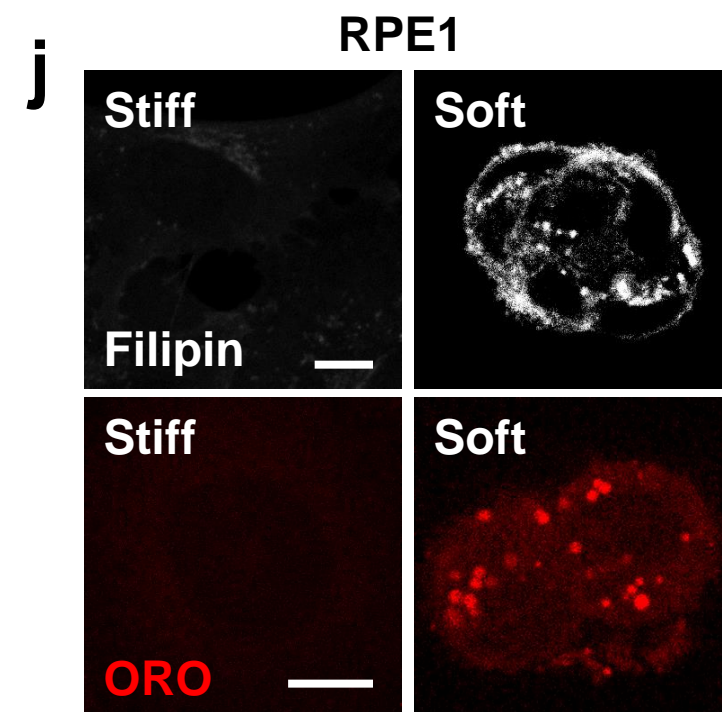
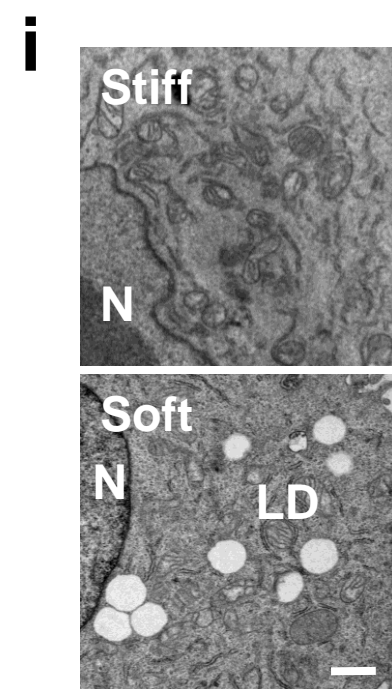
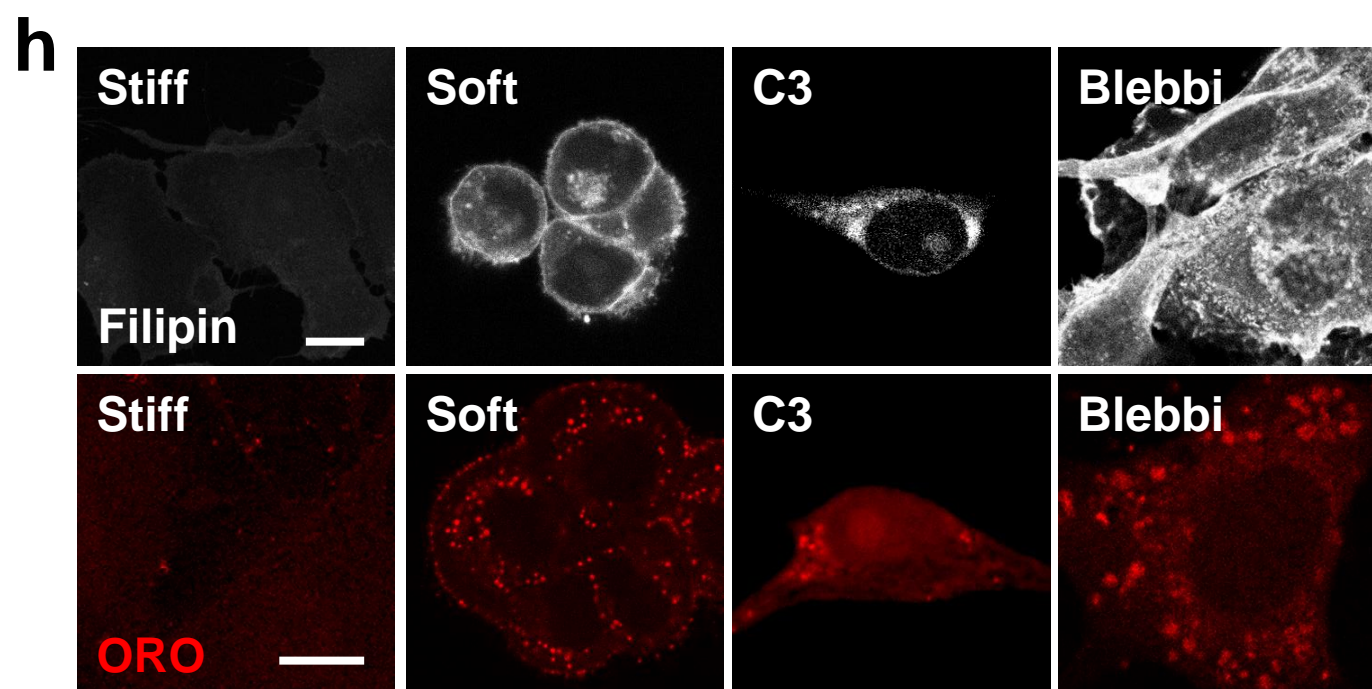
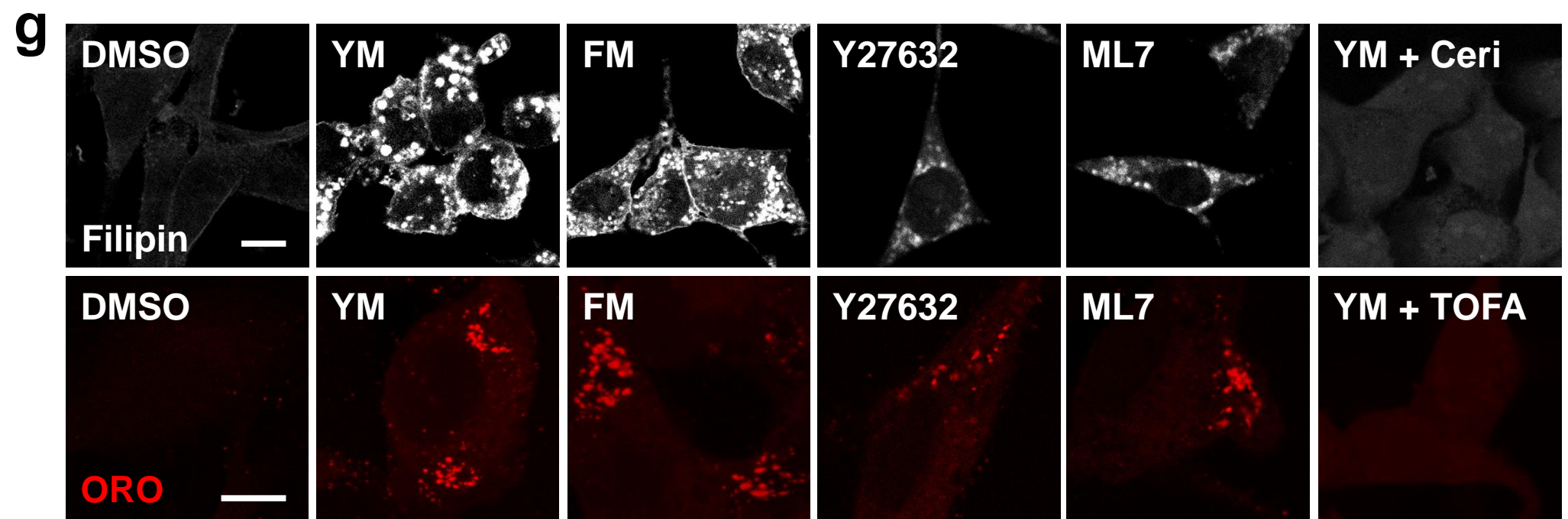
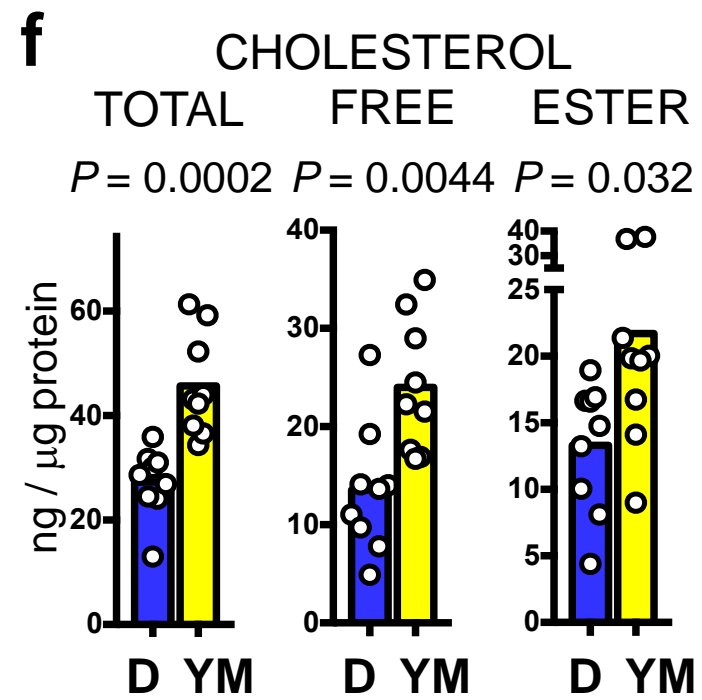
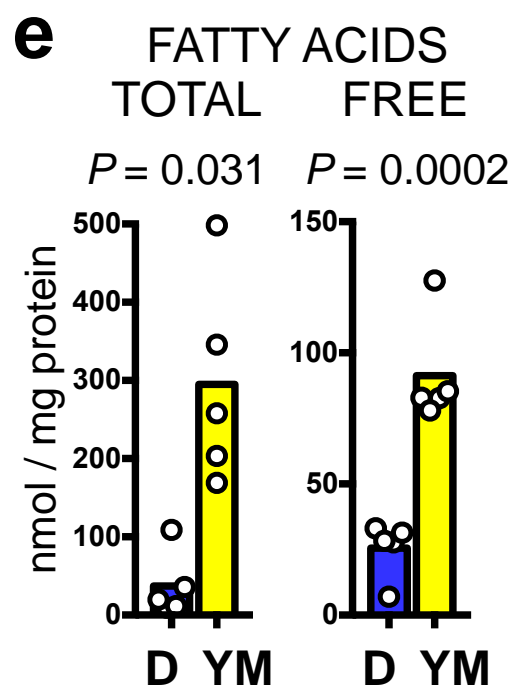
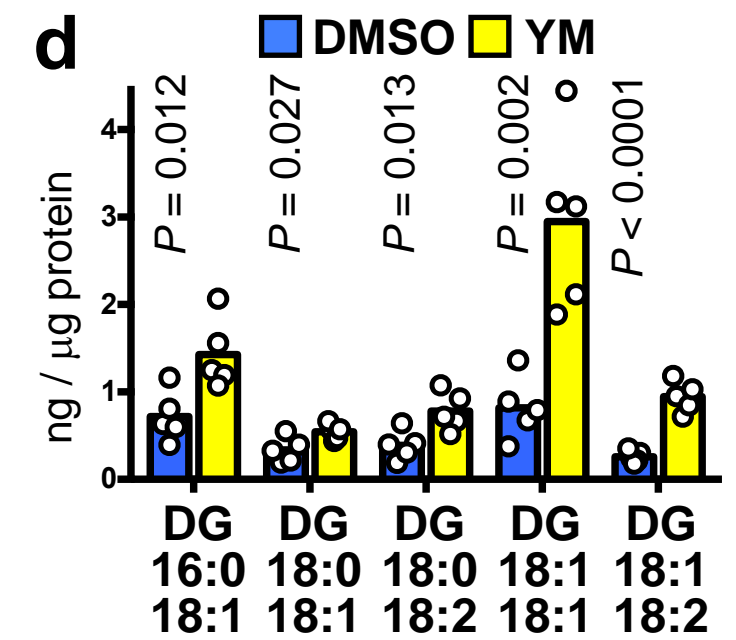
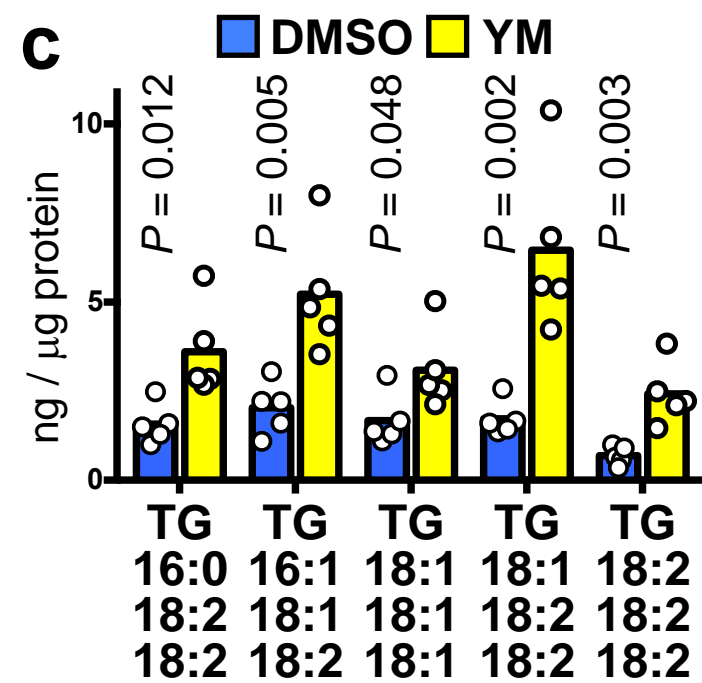
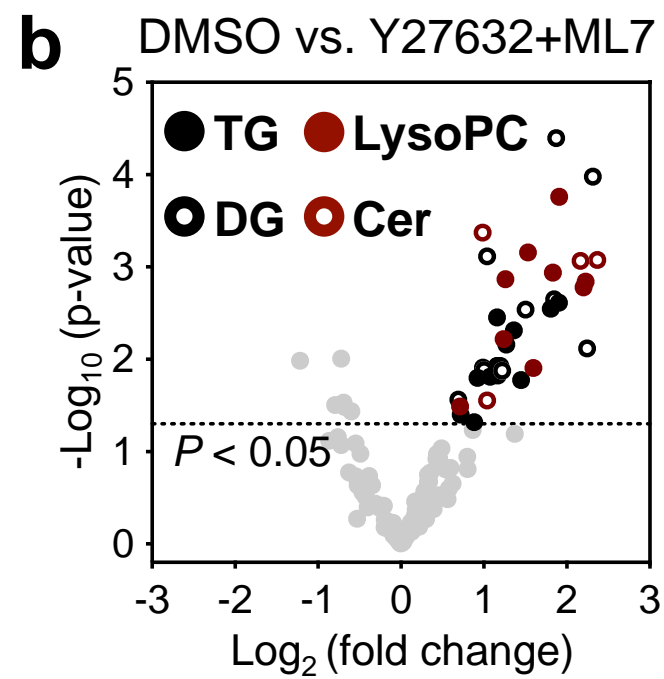
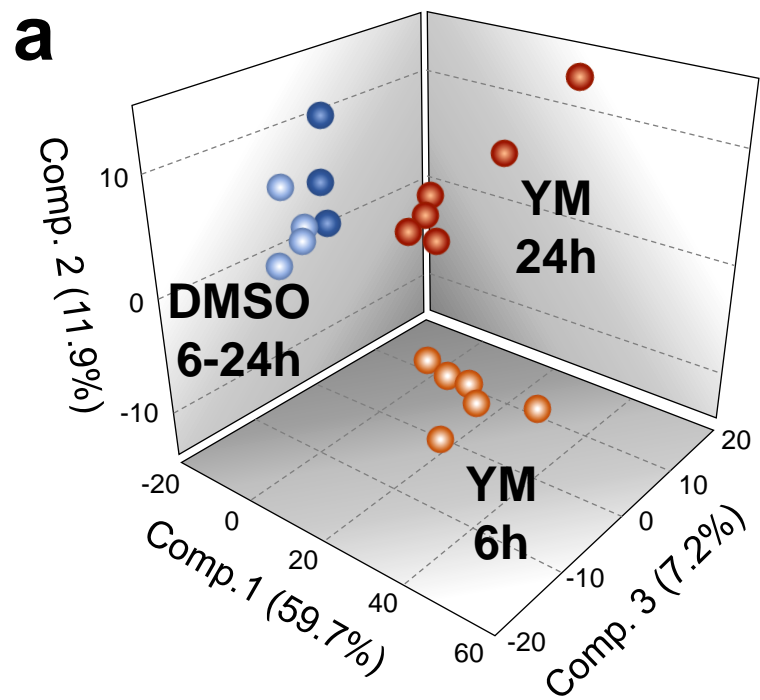
247  
248 **Statistics and Reproducibility.** All data are based on independent experiments with independent  
249 biological replicates, except for metabolomics and microarrays that were based on independent  
250 biological replicates harvested in a single experiment. Experimental repetitions were carried out by  
251 thawing a new aliquot of cells, deriving from the original stock. Key data were independently  
252 replicated by two different operators, across different cell lines, and with independent techniques  
253 providing coherent results. All  $n$  values are pooled between independent experiments. Data are  
254 presented as mean and single points, or mean and standard error of the mean (s.e.m.) as indicated in the  
255 figure legends. Significance tests were unpaired non-parametric Mann-Whitney tests, unpaired two-  
256 tailed Student's  $t$ -tests, multiple unpaired two-tailed Student's  $t$ -tests with Holm-Sidak correction (for  
257 analysis of multiple qPCR markers), or Welch's two sample  $t$ -tests (for global metabolomics).  $t$ -tests  
258 have been performed under the reasonable assumption that values follow a normal distribution and  
259 have similar variance.

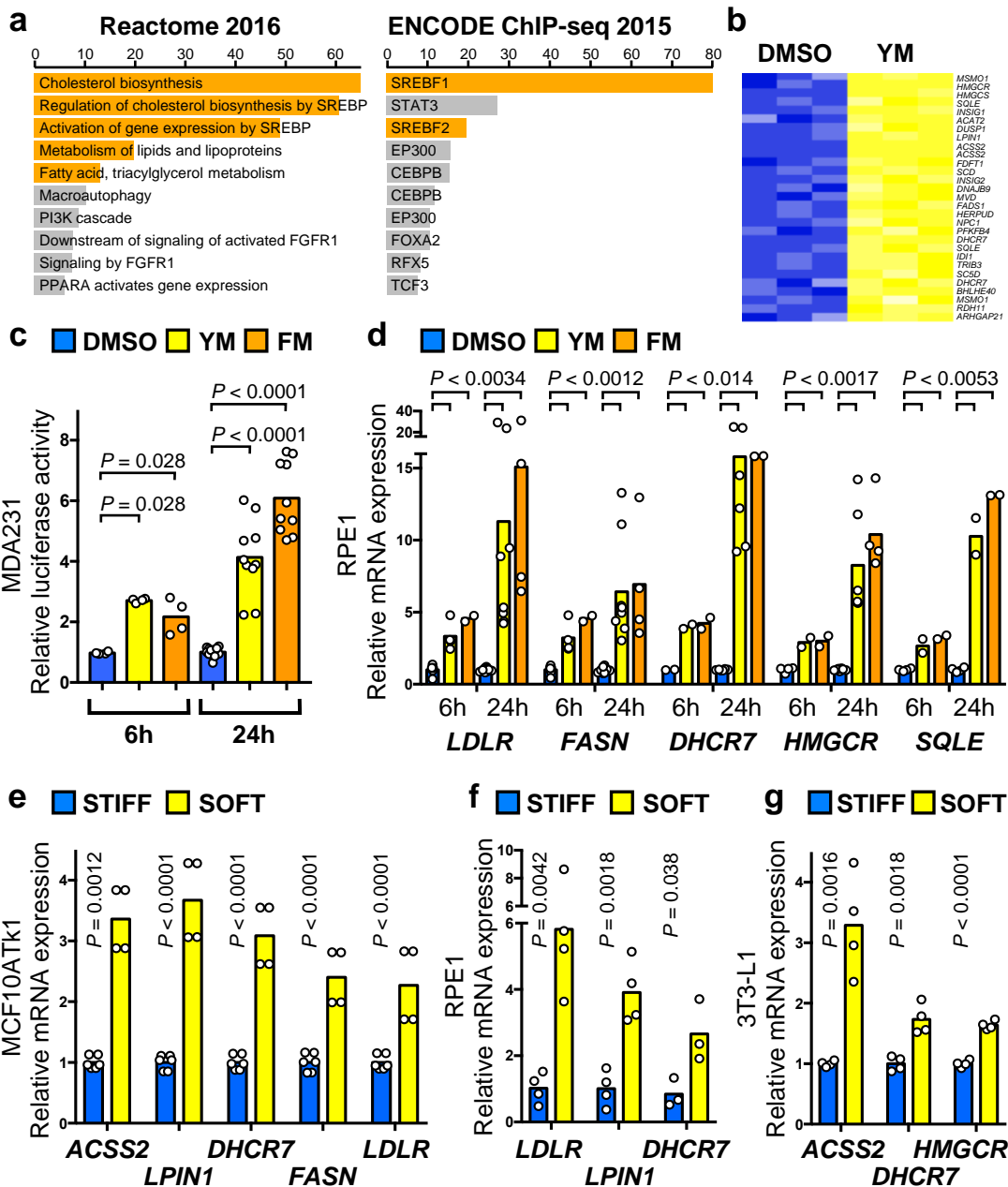
#### 260 **Code availability**

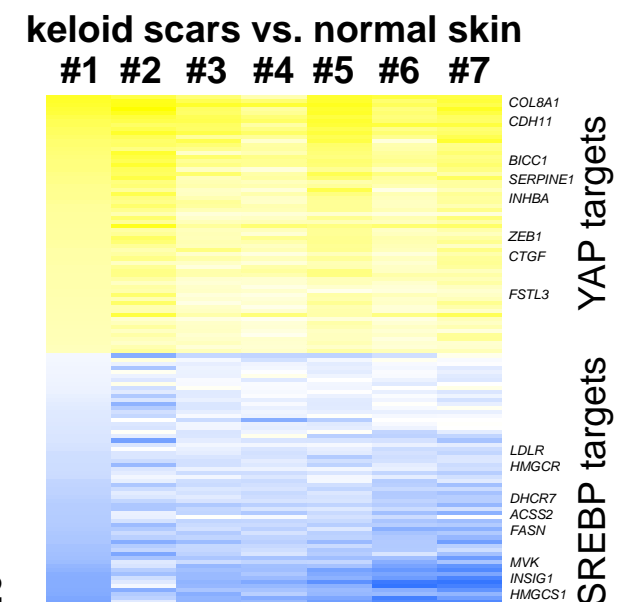
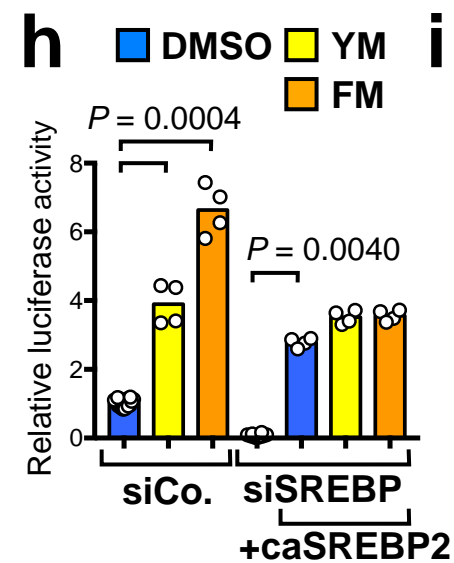
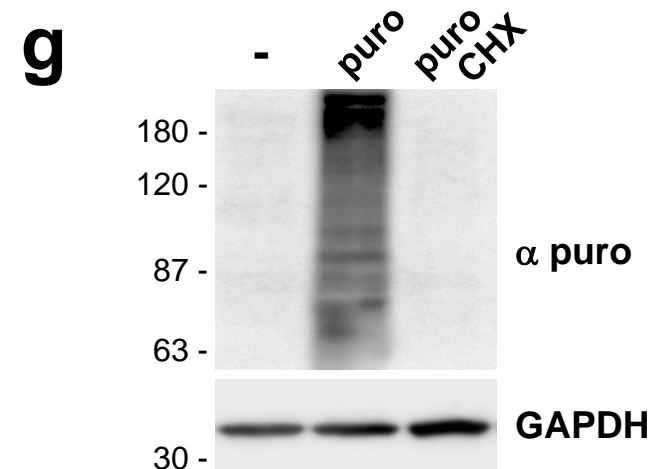
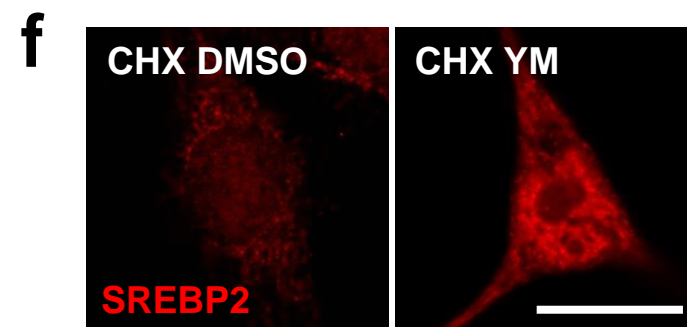
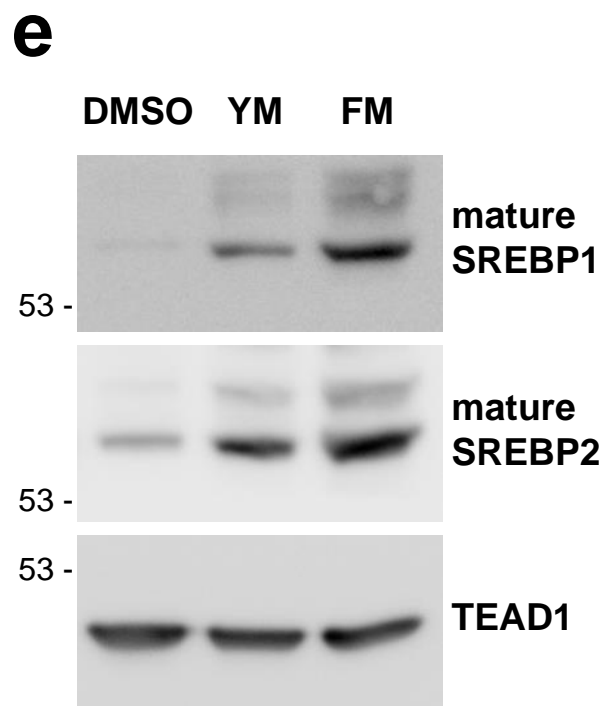
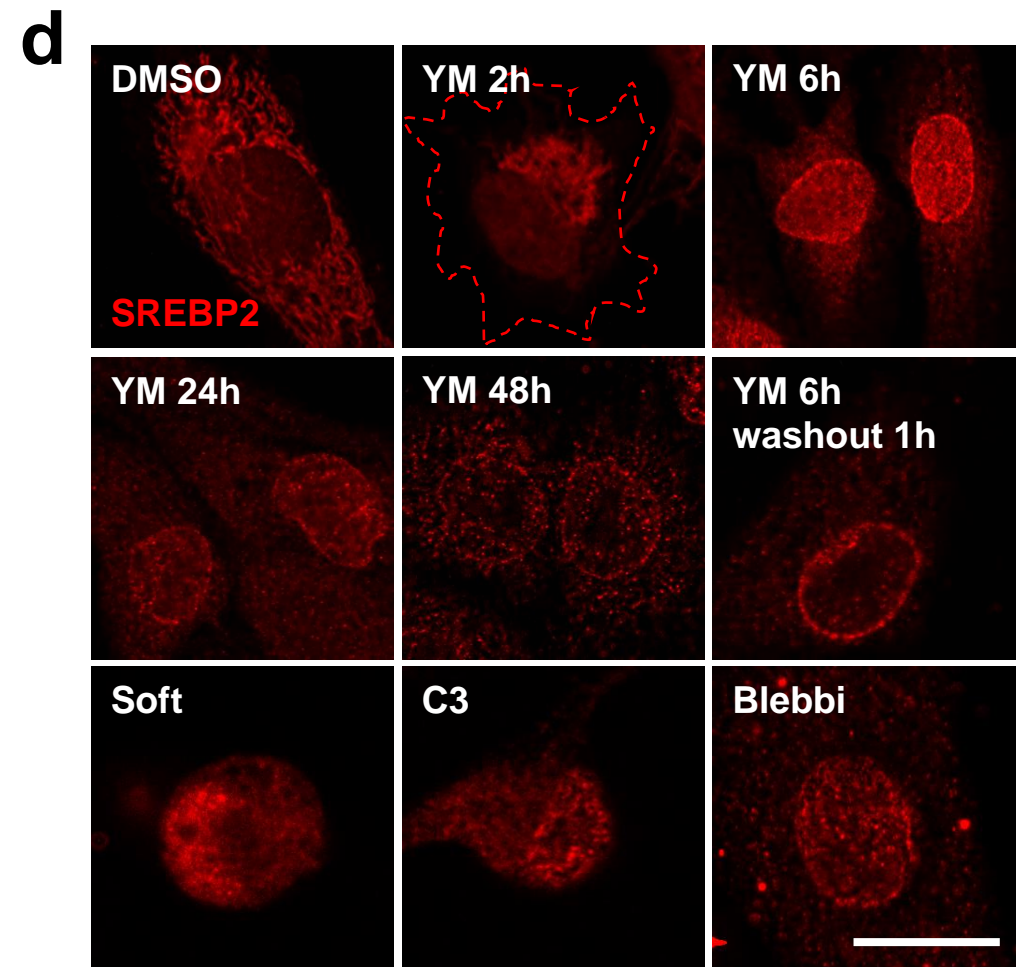
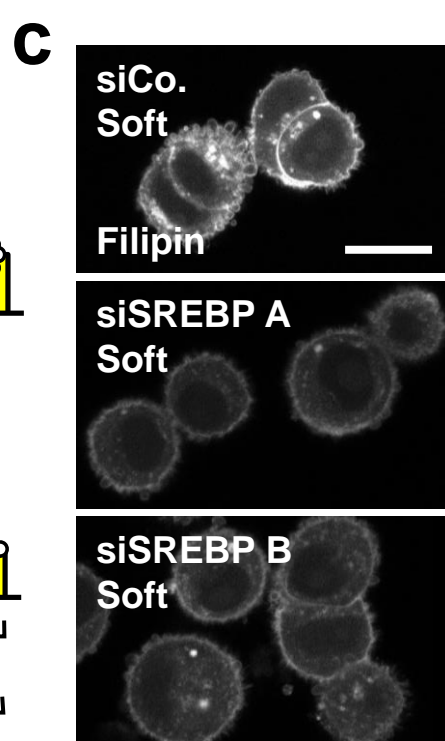
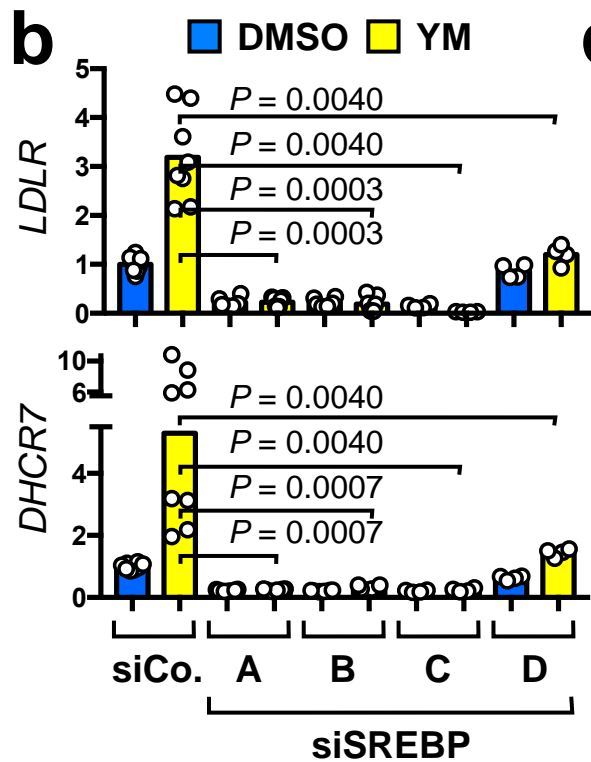
261 No custom codes were used in this study. All other codes are indicated in the appropriate methods  
262 sections and references.

263  
264  
265 **Data availability.** Microarray, metabolomics and targeted lipidomics data have been deposited (GEO  
266 database GSE107275 and Figshare database 10.6084/m9.figshare.7338764). Source data for Figs. **1-7**  
267 and Supplementary Figs. **1-7** have been provided in Supplementary Table **2**. All other data supporting  
268 the findings of this study are available from the corresponding author on reasonable request.

269

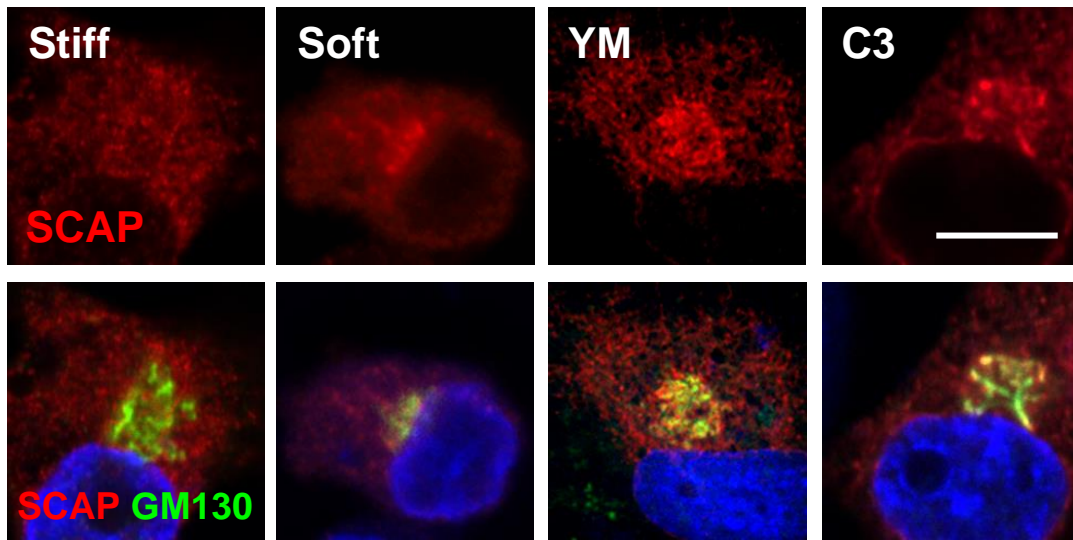




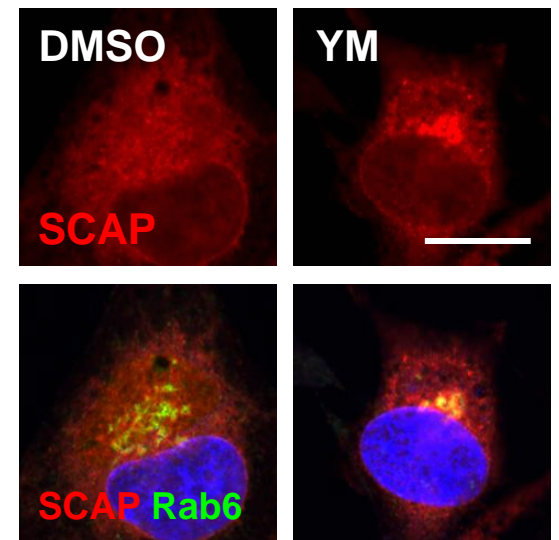
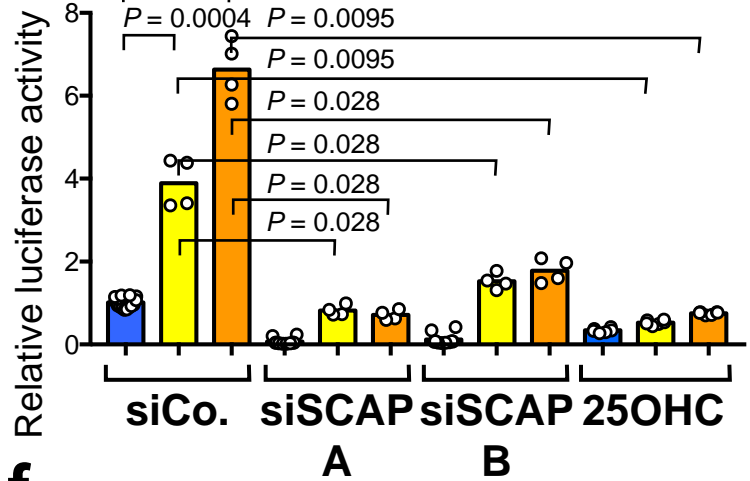
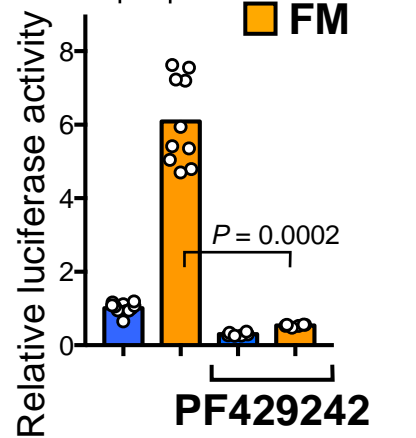
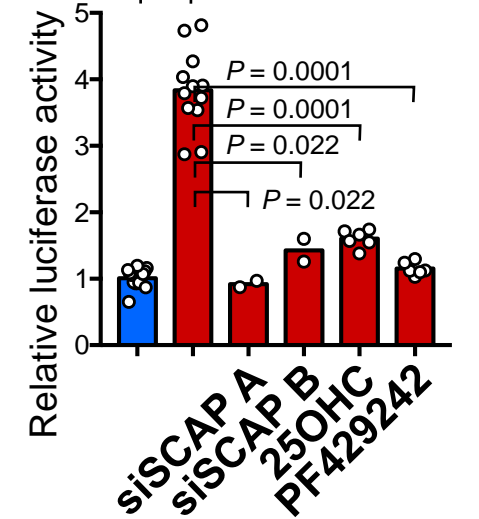
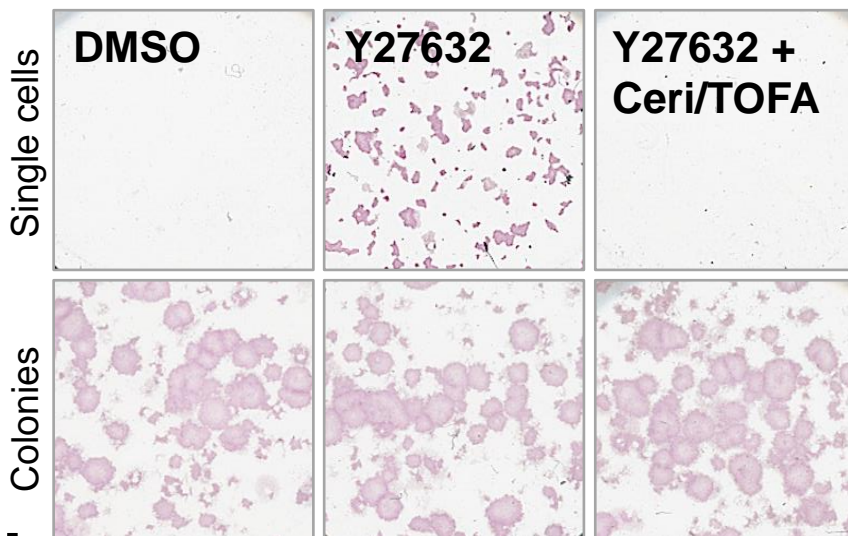
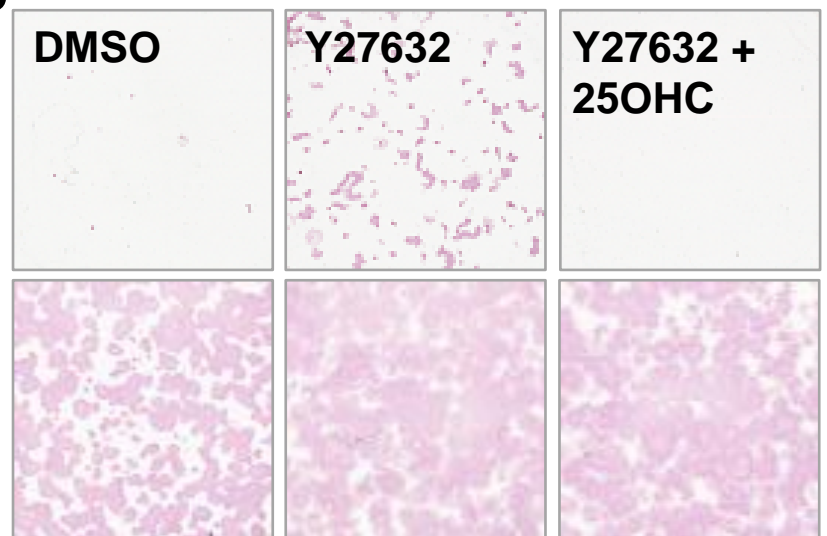


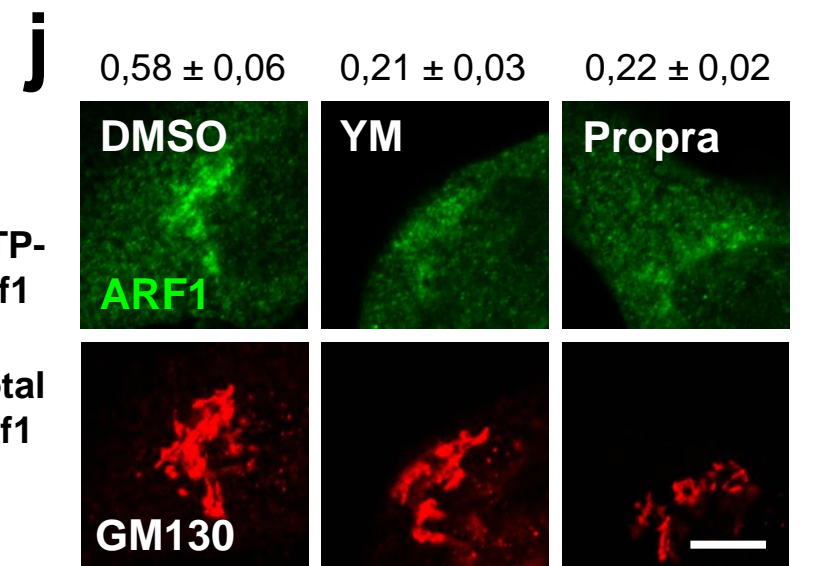
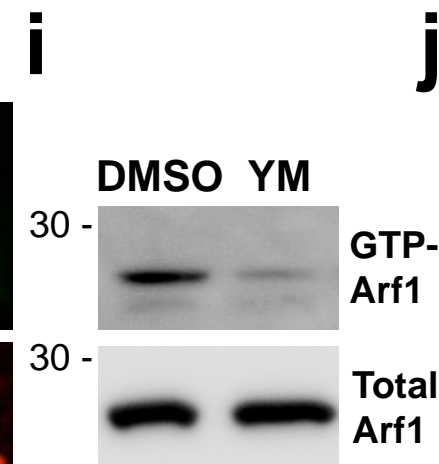
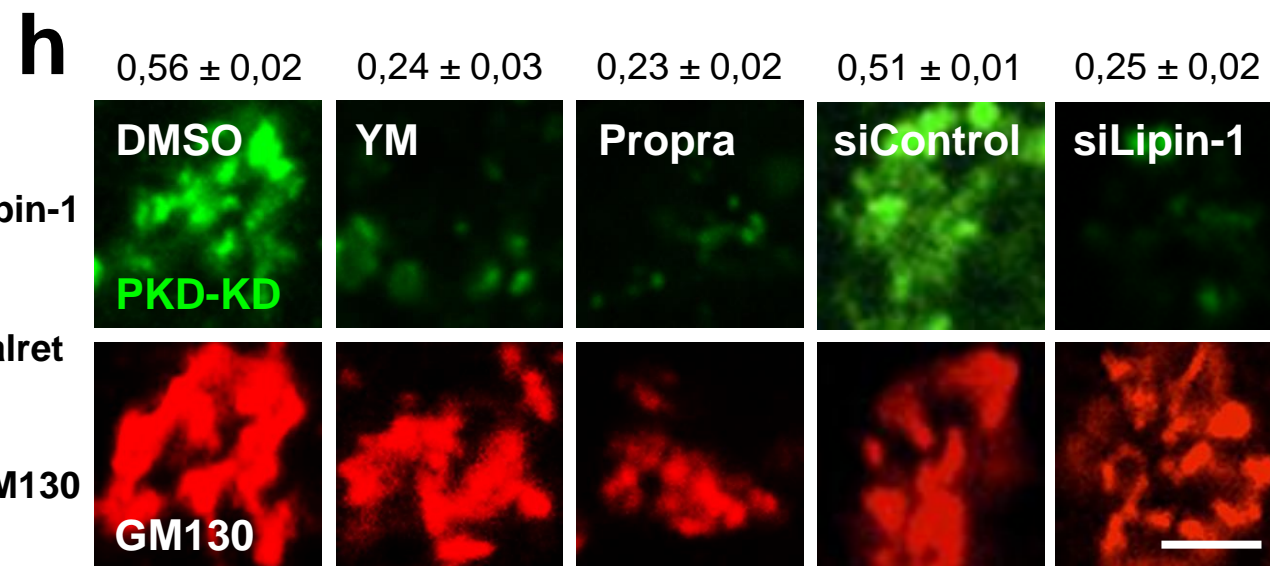
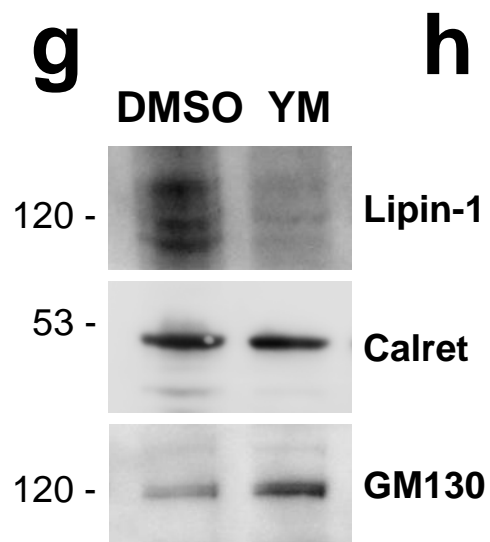
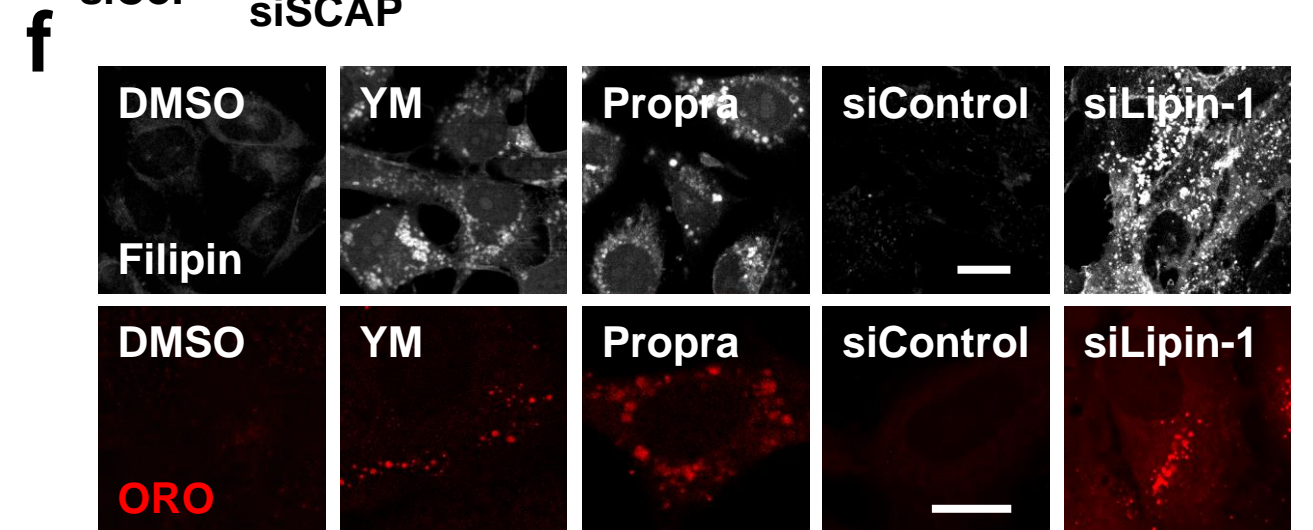
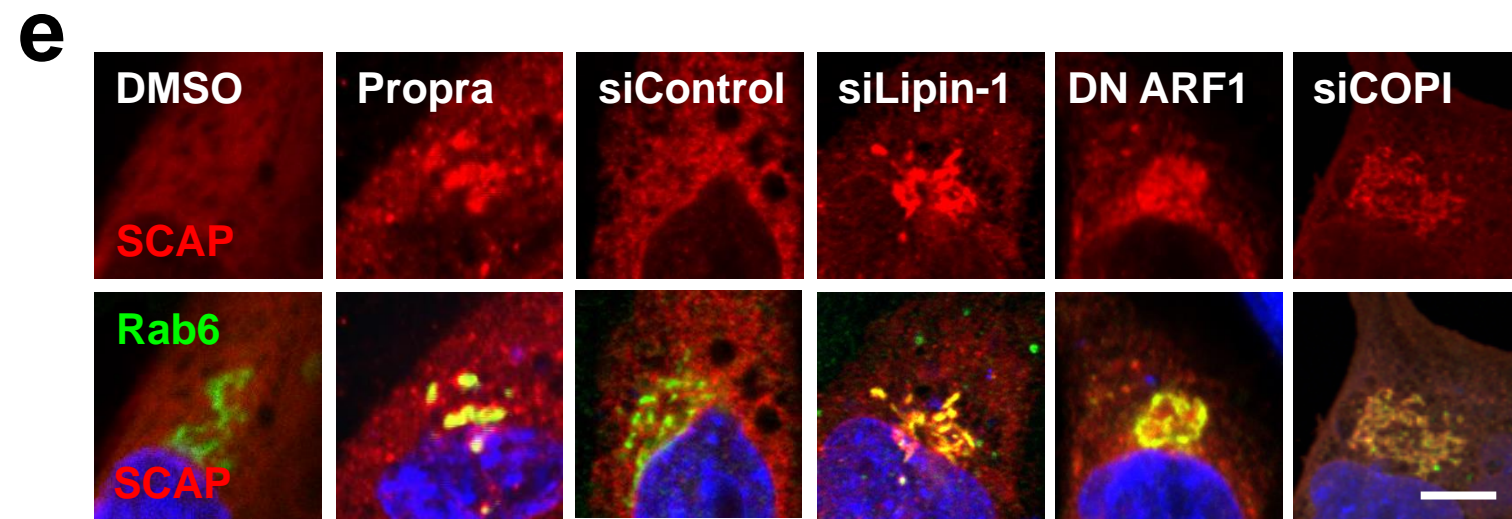
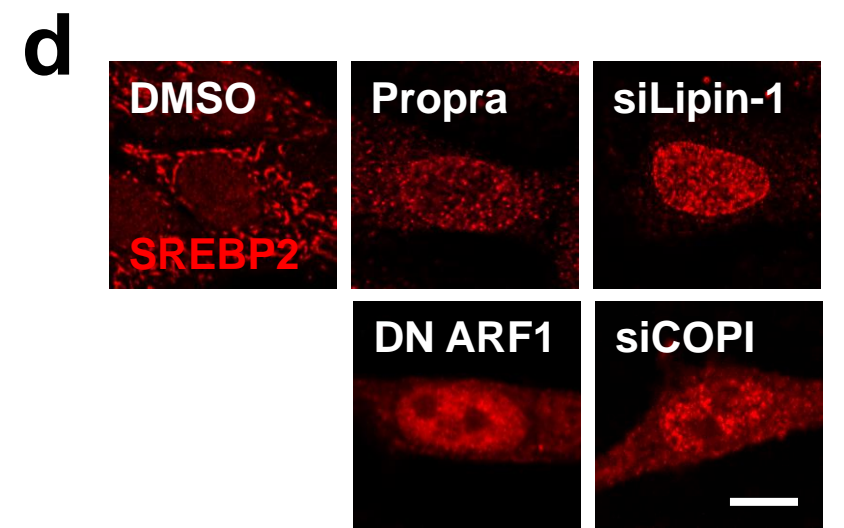
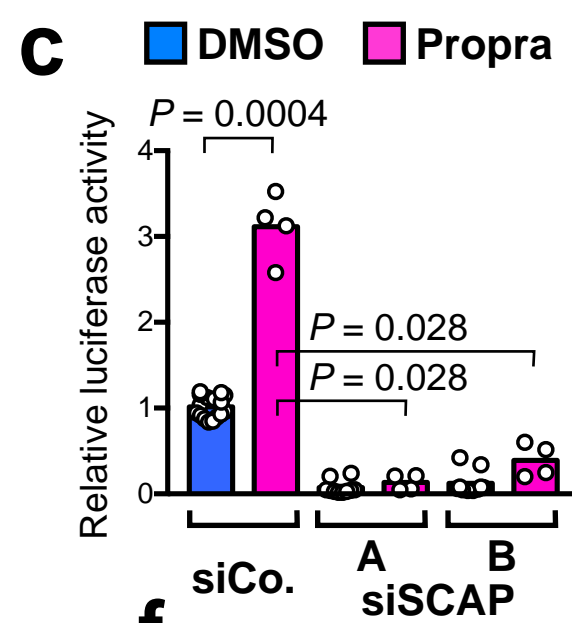
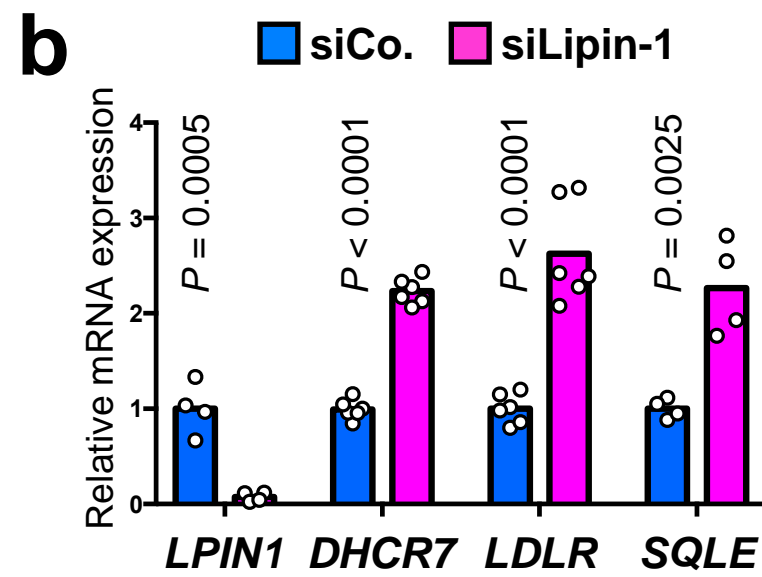
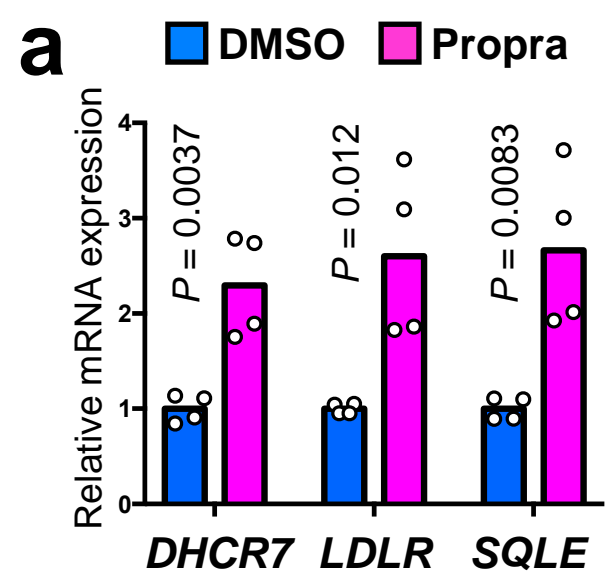
**a**

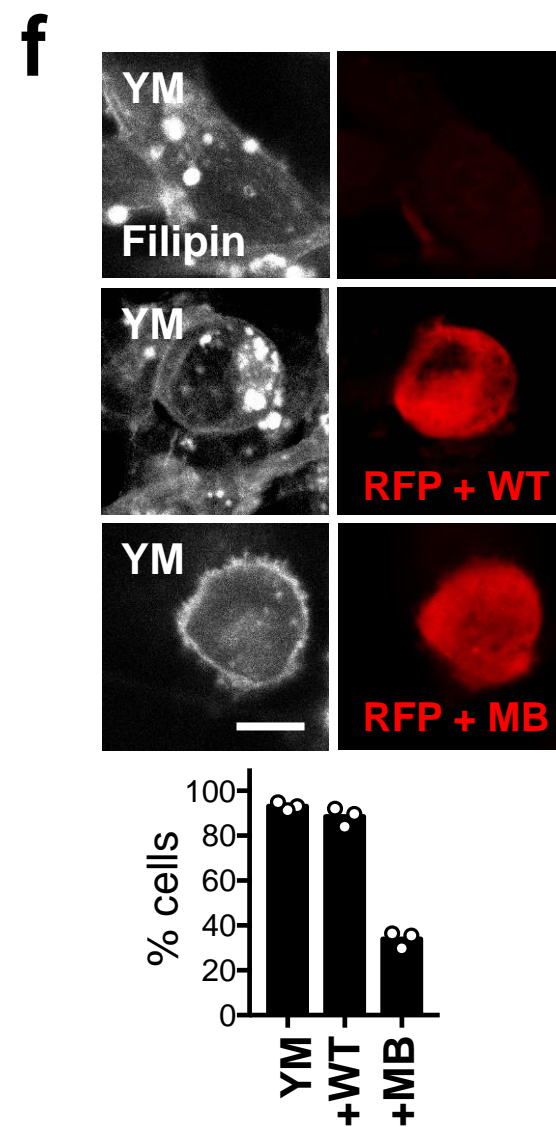
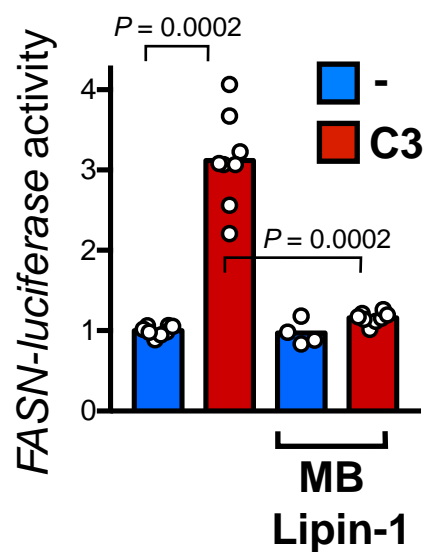
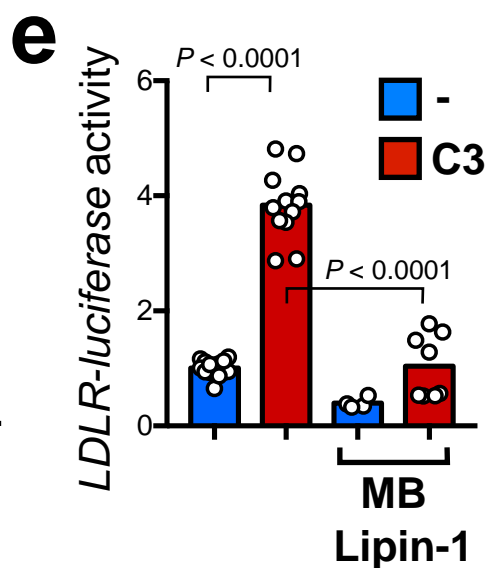
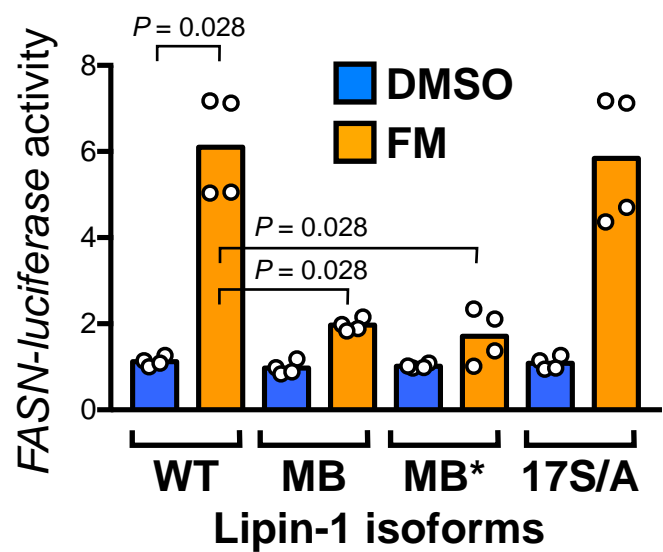
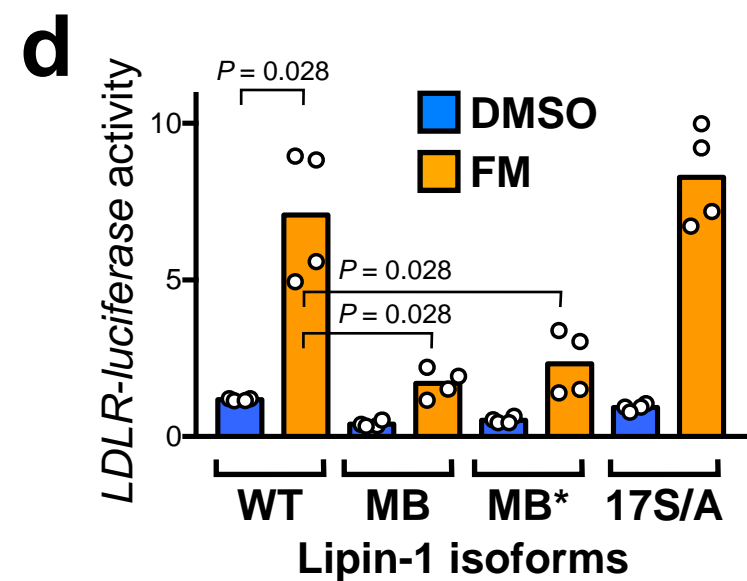
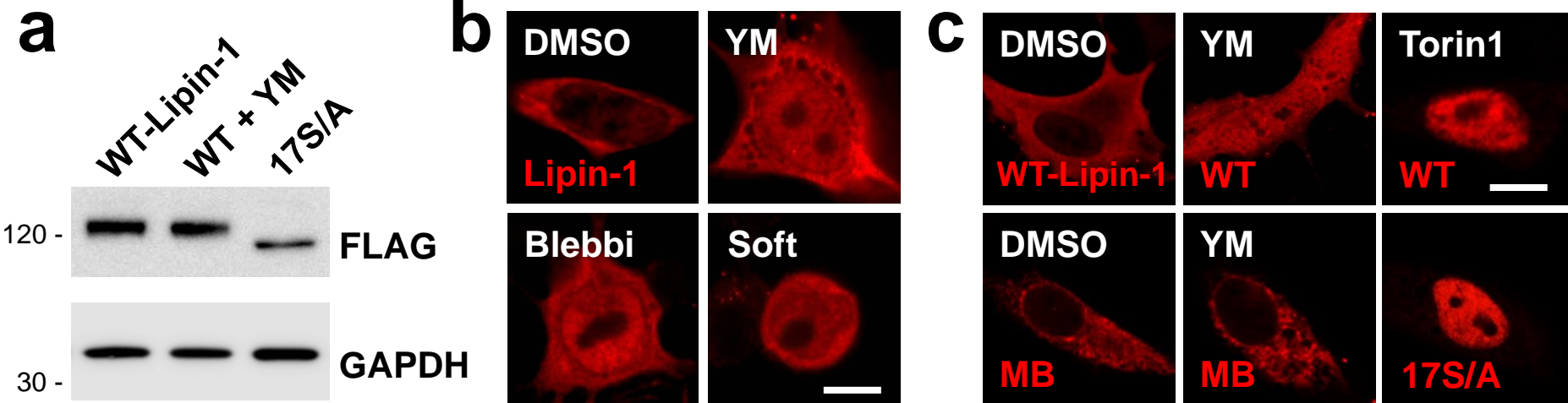
MCF10ATk1

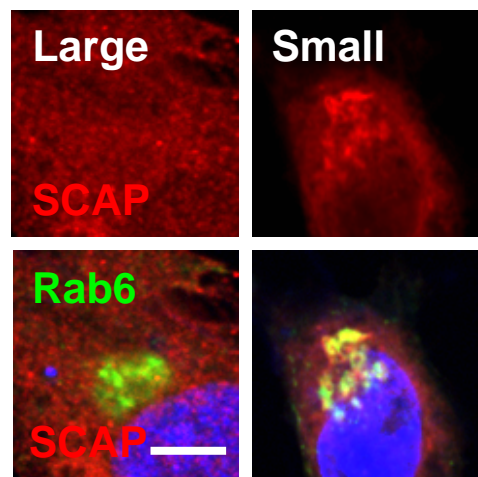
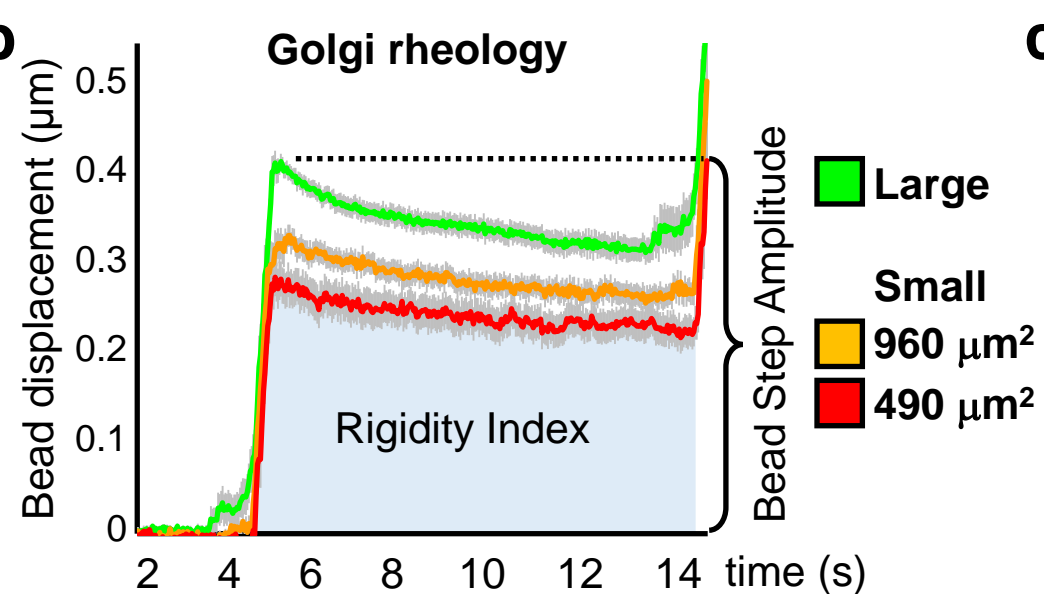
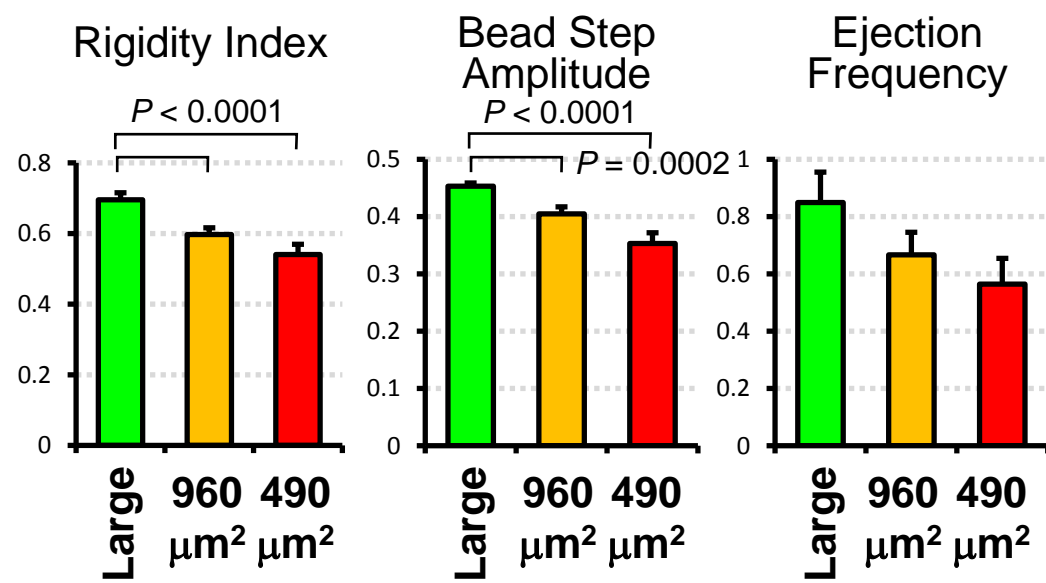
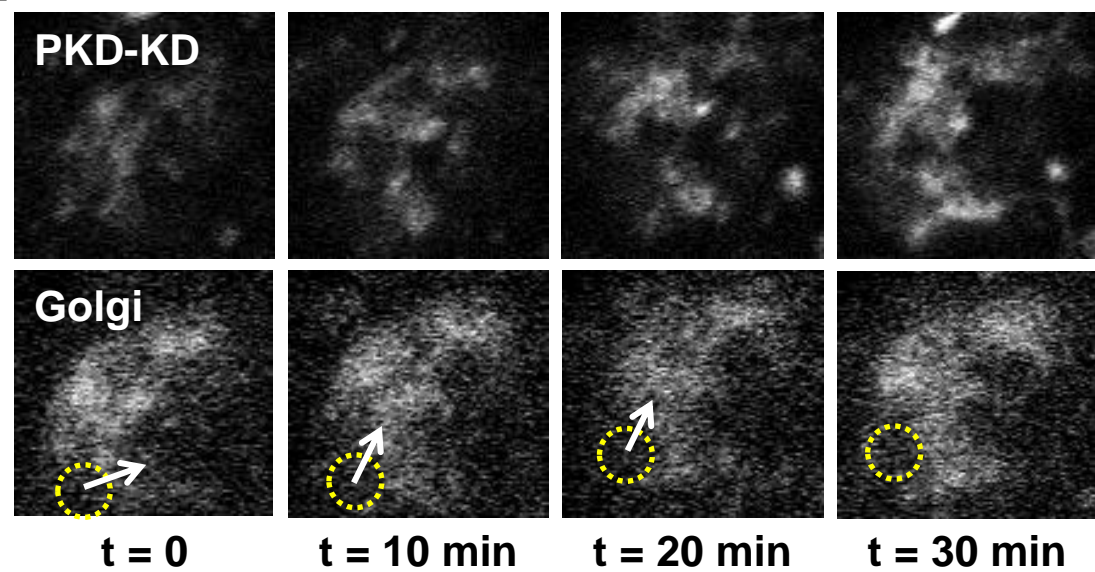
**b**

RPE1

**c****d****e****f****g****h**





**a****b****c****d****e**